Plasmodesmata act as unconventional membrane contact sites regulating inter-cellular molecular exchange in plants

Jessica Pérez-Sancho#[1], Marija Smokvarska#[1], Marie Glavier[1], Sujith Sritharan[2], Gwennogan Dubois[3], Victor Dietrich[1], Matthieu Pierre Platre[4], Ziqiang Patrick Li[1], Andrea Paterlini[1,5], Hortense Moreau[1], Laetitia Fouillen[1], Magali S. Grison[1], Pepe Cana-Quijada[1], Tatiana Sousa Moraes[1], Françoise Immel[1], Valerie Wattelet[1], Mathieu Ducros[6], Lysiane Brocard[6], Clément Chambaud[1,6], Matej Zabrady[10], Yongming Luo[7,8], Wolfgang Busch[4], Jens Tilsner[10], Yrjö Helariutta[5,9], Jenny Russinova[7,8], Antoine Taly[2], Yvon Jaillais[3]*, Emmanuelle M. Bayer[1,11]*.

[1] Laboratoire de Biogenèse Membranaire, UMR5200, CNRS, Université de Bordeaux, Villenave d'Ornon, France.
[2] Laboratoire de Biochimie Théorique, UPR9080, CNRS, Université Paris Cité, Paris, France.
[3] Laboratoire Reproduction et Développement des Plantes, Université de Lyon, ENS de Lyon, UCB Lyon 1, CNRS, INRA, F-69342 Lyon, France.
[4] Salk Institute For Biological Studies, Plant Molecular and Cellular Biology Laboratory, 10010 North Torrey Pines Road, La Jolla, CA 92037, USA.
[5] The Sainsbury Laboratory, University of Cambridge, Cambridge, UK.
[6] Bordeaux Imaging Centre, Plant Imaging Platform, UMS 3420, INRA-CNRS-INSERM-University of Bordeaux, Villenave-d'Ornon, France.
[7] Department of Plant Biotechnology and Bioinformatics, Ghent University, 9052 Ghent, Belgium.
[8] Center for Plant Systems Biology, VIB, 9052 Ghent, Belgium.
[9] Institute of Biotechnology, HiLIFE/Organismal and Evolutionary Biology Research Programme, Faculty of Biological and Environmental Sciences, Viikki Plant Science Centre, University of Helsinki, Helsinki, Finland.
[10] Biomedical Sciences Research Complex, University of St Andrews, Fife KY16 9ST, UK
Cell and Molecular Sciences, The James Hutton Institute, Dundee DD2 5DA, UK
[11] Lead contact: emmanuelle.bayer@u-bordeaux.fr (E.M.B.)

 # These authors equally contributed to the work
*** Correspondence:** yvon.jaillais@ens-lyon.fr (Y.J.), emmanuelle.bayer@u-bordeaux.fr (E.M.B.)

In brief

Plant intercellular communication is regulated via tubular membrane contact through PI4P binding-ER-PM tether MCTP proteins

Highlights (4 highlights / 85 characters max)

1- Plasmodesmata are unconventional ER/PM tubular contact sites sitting at cell-cell interface

2- Plasmodesmata act as control valves, adjusting the ER-PM contacts to modulate cytosolic flow

3- MCTP3, MCTP4, MCTP6 and PI4P tethering elements act as valve-size controllers

4- MCTP/PI4P tethers function independently of callose levels to regulate cell-to-cell diffusion

SUMMARY

Membrane contact sites (MCSs) are fundamental actors of intracellular communication, but their role in intercellular communication remains unexplored. Here we show that in plants, plasmodesmata cytoplasmic bridges function as atypical endoplasmic reticulum (ER)-plasma membrane (PM) tubular MCSs, operating at cell-cell interfaces. Similar to other MCSs, ER-PM apposition within plasmodesmata is controlled by a protein-lipid tethering complex. Unlike other MCS however, regulation of membrane contacts primarily serves intercellular communication. Plasmodesmata MCSs act as flow-control valves, effectively regulating molecular transport between cells, by modulating the ER-PM passage size. This occurs through the collaborative action of the ER-anchored Multiple C2 domains and transmembrane domain proteins (MCTP) 3, 4, and 6 tether-complex, and PM-localized PI4P lipid as a binding partner. The MCS flow-control mechanism overrides the well-established plasmodesmata regulator callose, rendering plasmodesmata unable to close in MCTPs absence. Our findings highlight MCS's diversified functions in transmitting information, spanning from intracellular to intercellular cellular activities.

INTRODUCTION

Recent years have seen a paradigm shift in our understanding of intracellular communication with the discovery of membrane contact sites (MCSs) (Scorrano et al., 2019; Prinz et al., 2020). By mediating close contacts between two membranes, MCS act as specialized platforms for inter-organellar exchanges, enabling transfer of ions and other molecules (Soboloff et al., 2006; Mesmin et al., 2013; Schauder et al., 2014; Chung et al., 2015; von Filseck et al., 2015; Eden et al., 2016; Wong et al., 2016; Wilhelm et al., 2017; Balla, 2018; Bian et al., 2018; Kumagai and Hanada, 2019; Ruiz-Lopez et al., 2021; Qian et al., 2022; Radulovic et al., 2022; Guillén-Samander and De Camilli, 2023; Naón et al., 2023; Wozny et al., 2023). This direct molecular transfer between organelles involves specialized protein machinery and membrane proximity regulation (Scorrano et al., 2019). Interest in MCS has grown dramatically in the last decade, with a shift of focus from describing their molecular composition to understanding their functions. Besides inter-organellar communication, MCS were shown to be involved in organelle biogenesis, fission and trafficking, cargo sorting, cellular stress responses, and autophagy; highlighting the functional diversity of these eukaryotic structures (Eden et al., 2010; Friedman et al., 2011; Hamasaki et al., 2013; Rowland et al., 2014; Pérez-Sancho et al., 2015; Dong et al., 2016; Hirabayashi et al., 2017; Lees et al., 2017; Collado et al., 2019; Hernández-Alvarez et al., 2019; Hoffmann et al., 2019; Lee et al., 2019; Wang et al., 2019; Ruiz-Lopez et al., 2021). It is now clear that every organelle inside a single cell forms functional contacts, and that MCS activities are not only broad but also vital for the cell.

While MCS are now well-established essential contributors to intracellular coordination, many multicellular eukaryotic organisms require effective communication that extends beyond organelles and includes communication between individual cells. So far, our understanding of MCS function primarily pertains to intracellular activities, and there is currently no evidence supporting the notion that MCS facilitate direct molecular exchange between cells.

With this shift in mind, we addressed the possible functions of MCS in inter-cellular (as opposed to inter-organellar) molecular exchange. Among eukaryotic cells, the endoplasmic reticulum (ER) serves as a central hub for MCSs, forming multiple contacts with various organelles (Salvador-Gallego et al., 2017; Wu et al., 2018a). In most eukaryotic cells the ER is confined to a single cell. However, in land plants and some green algae, the ER network extends from cell-to-cell through communication bridges known as plasmodesmata (Nicolas et al., 2017b) (**Figure 1A**). Unlike desmosome cell-cell junctions or any other cell-cell contact dependent communication structures, both the ER and the PM traverse cell-cell boundaries through plasmodesmata junctions. Inside plasmodesmata the ER takes the form of a condensed membrane tube known as the desmotubule which comes in close apposition with the PM, creating an atypical tubular MCS-like structure (Ding et al., 1992; Tilsner et al., 2016; Nicolas et al., 2017a). Millions of plasmodesmata bridges weave through the plant body, allowing direct molecular exchange of nutrients and signaling molecules in the space between the ER and the PM, called the cytoplasmic sleeve (Deinum et al., 2019) (**Figure 1A**). These structures are pivotal for plant intercellular communication, allowing cells to coordinate their activities, exchange resources, and respond to environmental and developmental signals in a synchronized manner (Nakajima et al., 2001; Guseman et al., 2010; Benitez-Alfonso et al., 2013; Faulkner et al., 2013; Stahl et al., 2013; Wang et al., 2013; Daum et al., 2014; Vaddepalli et al., 2014; Otero et al., 2016; Stahl and Faulkner, 2016; Gaudioso-Pedraza et al., 2018; Tylewicz et al., 2018; Miyashima et al., 2019; Song et al., 2019; Tran et al., 2019; Gao et al., 2020; Mellor et al., 2020; Kitagawa et al., 2022; Mehra et al., 2022; Tee et al., 2022; Wang et al., 2023). Yet the molecular mechanisms regulating cell-cell molecular flow continue to evade complete understanding.

While plasmodesmata comply with the general definition of MCS: (1) area of close proximity between two membranes, (2) absence of membrane fusion, (3) site of specialized function and (4) defined proteome and lipidome (Li et al., 2021), we still do not know if they function as MCS. Their unique membrane organization has been known for decades and yet it is still not known whether plasmodesmata-driven cell-cell communication requires regulation of ER-PM contacts and if dysregulation of these contacts impacts the functionality of plasmodesmata. Until now, the local synthesis and degradation of a beta-1,3-glucan polymer (callose) in the wall around plasmodesmata, is the only characterized mechanism to regulate plasmodesmata permeability (Zavaliev et al., 2011; Amsbury et al., 2017; Wu et al., 2018b).

Given their position at cell-to-cell interfaces, we hypothesize that regulating ER-PM tethering at plasmodesmata functions as a mechanism to modulate the diffusion of cytoplasmic components between neighboring cells. This mechanism would stand as the first example in eucaryotes of MCS driven-intercellular communication. In this work, we undertook to identify the molecular actors by which plasmodesmata may control the exchange of information among cells by regulating MCS, with a focus on the model plant *Arabidopsis thaliana.*

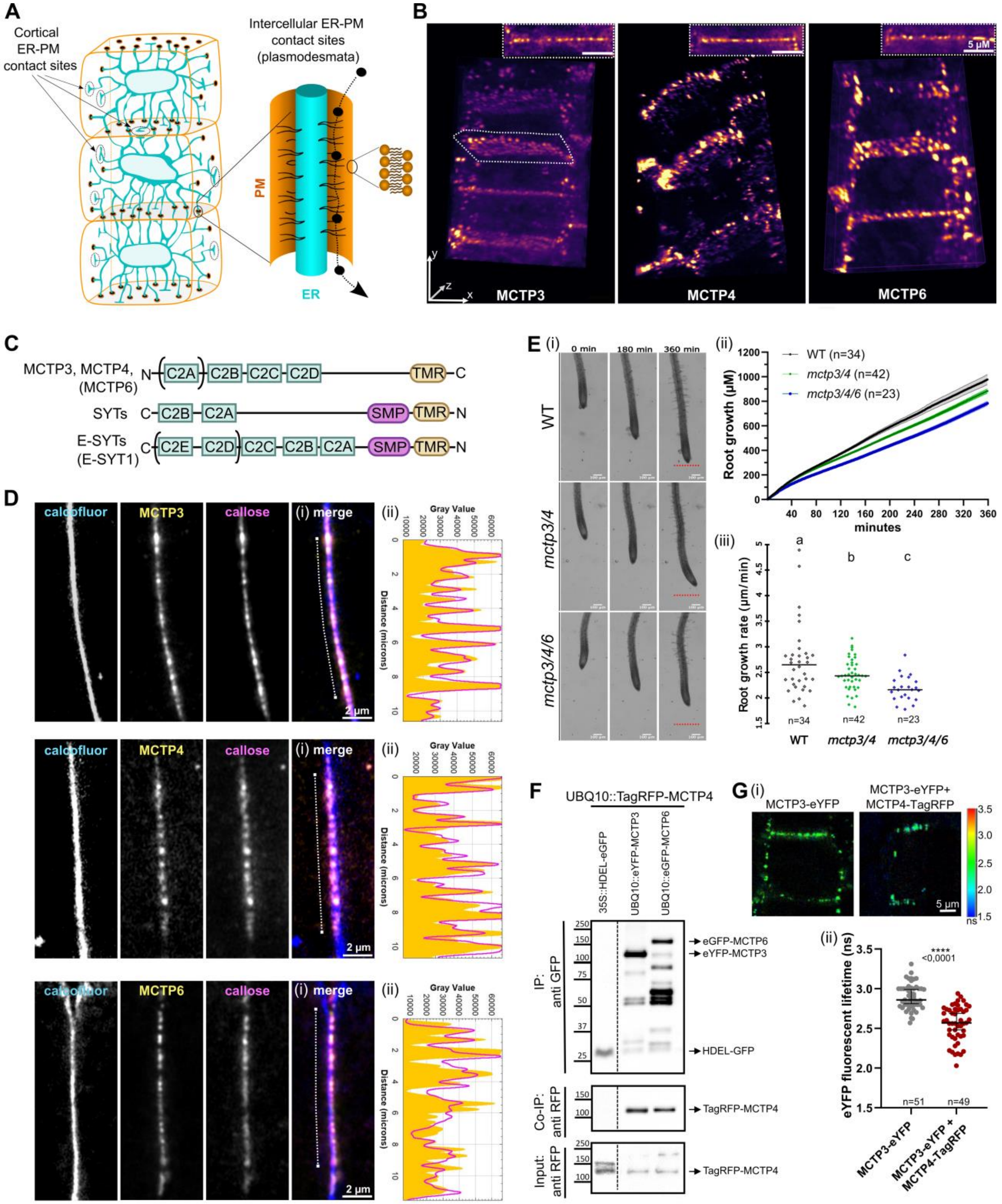

Figure 1. Plasmodesmata localized MCTP3, MCTP4 and MCTP6 show physical and genetic interaction.
(A) Schematic representation of ER-PM contact sites in plants.
(B) 3D view of *mctp3/4* p*UBQ10::eYFP MCTP3*, *mctp3/4* p*UBQ10::eYFP-MCTP4* and *mctp3/4* pUBQ10::MCTP6-mVenus acquired with lattice light-sheet microscopy. Insets represent one focal plane from the lattice light-sheet set.
(C) Schematic representation of ER-PM contact site protein tethers MCTPs (plants), Syntaptotagmins (plants) and E-Synaptotagmins (mammals) depicting phospholipid-binding C2 domains, lipid-transfer SMP domains and

transmembrane regions (TMR). Please note that the size of the domains and the distances between them is not to scale.
(D) Confocal micrographs of *mctp3* p*MCTP3*::eYFP-MCTP3, *mctp4* p*MCTP4*::eYFP-MCTP4 and *mctp6* p*MCTP6*::MCTP6-mVenus co-immunolocalized with callose by anti-callose immunostaining (i). Calcofluor-white is used to visualize cell walls. Intensity plots (ii) show YFP/mVenus (yellow) and atto594 (callose, magenta) intensity values along the wall in (i).
(E) Root growth assay of WT, *mctp3/4* and *mctp3/4/6* continuously imaged for 360 minutes. (i). Representative images at the indicated time points.The red line marks the length of the WT root, for comparison with the mutants (ii). Quantification of root growth over time. (iii). Quantification of the root growth rate in µm/minutes. Number of plants per condition indicated in the figure. Statistical analysis was done with ANOVA followed by Tukey's test. Line indicates median. Root growth assays were repeated 3 times with similar results.
(F) Western blot showing co-immunoprecipitation with GFP-Trap® beads in *Nicotiana benthamiana* plants transiently expressing p*UBQ10::TagRFP-MCTP4* as bait and p*35S::HDEL-GFP*, p*UBQ10::eYFP-MCTP3* or p*35S::eGFP-MCTP6* as pray proteins. Each sample consists on 40 leaf-discs extracted from 3 plants, 2 leaves per plant. Experiment was repeated 3 times with similar results.
(G) Fluorescence lifetime of *mctp3/4/6* plants expressing *pMCTP3::eYFP-MCTP3* as donor alone or with *pMCTP4::tagRFP-MCTP4* as acceptor. (i). Representative images with color-coded fluorescent lifetime per pixel in nanoseconds (ns). (ii). Quantification of fluorescent lifetime. 3-4 plants were used per condition, 2-3 images were taken per plant and several ROIs (total indicated in the figure) were measured per image. Statistical analysis was done with Student t-test. Line indicates median, error bars indicate 95% confidence index (CI). Experiment was repeated twice with similar results and data were pooled together.
In this figure and throughout all the figures in the paper, *mctp3/4* stands for *mctp3-2 mctp4-1* and *mctp3/4/6* stands for *mctp3-2 mctp4-1 mctp6-1.*

RESULTS

MCTP3, MCTP4 and MCTP6 form a tethering complex at plasmodesmata and redundantly impact plant growth and development

Plasmodesmata are dynamic nanoscopic structures with the capacity to dilate and contract, acting as checkpoints controlling cell-to-cell trafficking. Sitting at the cell-cell interface, they have the potential to combine membrane contact regulation with intercellular functions. In such a scenario, MCS would act as a valve controlling the molecular flow by adjusting the ER-PM gap (**Figure 1A**). To test if ER-PM apposition is functionally relevant for plasmodesmata function, we targeted the molecular machinery controlling it. MCSs are regulated by protein tethers which physically bridge the two membranes (Scorrano et al., 2019). We previously identified a family of putative ER/PM tethers called Multiple C2 domains and transmembrane domain proteins (MCTPs) that localize specifically at plasmodesmata (Brault et al., 2019). Several plasmodesmata proteomes from different species from moss to vascular plants have been published over the last few years. By cross referencing *Arabidopsis thaliana* (Arabidopsis) (Fernandez-Calvino et al., 2011; Brault et al., 2019), *Populus trichocarpa* (Leijon et al., 2018) and *Nicotiana benthamiana* (Kraner et al., 2017) plasmodesmata proteomes, Miras et al.(Miras et al., 2022b) identified 20 core plasmodesmata proteins out of which MCTP proteins are represented. Furthermore, using phyloproteomics, Johnston *et al.*(Johnston et al., 2023) identified three conserved plasmodesmata protein families, among them the MCTP family.

We therefore selected MCTPs as ER-PM tether candidates and proceeded to evaluate their function in cell-cell trafficking in the model plant *Arabidopsis thaliana*. MCTPs are structurally related to the MCS tethers Extended-synaptotagmins (E-Syts) in animal and Synaptotagmins (SYTs) in plant (Giordano et al., 2013; Pérez-Sancho et al., 2015; Brault et al., 2019; Ruiz-Lopez et al., 2021) (**Figure 1C**). They consist of a C-terminal ER-anchor and three to four C2 lipid binding domains. In Arabidopsis, the MCTP family comprises 16 members, among which MCTP3, MCTP4, and MCTP6 were identified in plasmodesmata fractions in a systematic manner (Fernandez-Calvino et al., 2011; Kraner et al., 2017; Brault et al., 2019; Kirk et al., 2022; Miras et al., 2022a; Gombos et al., 2023; Johnston et al., 2023). Given that nearly all plant cells are interconnected by these communication bridges, it is anticipated that a primary component would be widely expressed and consistently associated with plasmodesmata, irrespective of tissue type or developmental stage. Analysis of publicly available gene expression profiling databases revealed that all three genes, MCTP3, MCTP4, and MCTP6, were widely and consistently expressed in both shoot and root tissues, with MCTP4 exhibiting the strongest expression levels (**Figure S1A** and **Fig S1B**). In all tissues examined, the proteins exhibited a dotty localization pattern at cell-cell interfaces, reminiscent of plasmodesmata localization (**Figure 1B; Figure S1C-E; Movie S1-3;** (Brault et al., 2019)). In previous work, we showed that MCTP4 localized at plasmodesmata when stably expressed under endogenous promoter in Arabidopsis (Brault et al., 2019). We further confirmed this finding for all three members using Airyscan imaging and co-localization with callose, a well-established plasmodesmata marker (**Figure 1D**). From these data, we concluded that MCTP3, MCTP4, and MCTP6 are widely expressed and genuine core constituents of plasmodesmata and therefore a suitable target for investigating plasmodesmata MCS function.

As MCTPs share homology with E-Syts and SYTs (Brault et al., 2019), which are known to form functionally relevant homotypic complexes at ER-PM MCS (Giordano et al., 2013; Ruiz-Lopez et al., 2021), we investigated whether MCTP3, MCTP4, and MCTP6 could potentially form a complex. We first examined their interaction at the genetic level by generating Arabidopsis loss-of-function mutants (single, double and triple mutant alleles). Plasmodesmata function in cell-to-cell communication is critical for plant growth and development, and disruption of master regulators is expected to induce strong and pleiotropic phenotypic defects. Single loss-of-function mutants (*mctp3-1*, *mctp3-2*, *mctp4-1*, *mctp4-2* or *mctp6-1*) presented no strong phenotypic anomaly (**Figure S2A-C, S3, S4)**. However, the double mutants involving MCTP4 loss-of-function (*mctp3-1/mctp4-1*, *mctp3-2/mctp4-1*, *mctp4-1/mctp6-1*) were severely affected in both shoot and root growth and development (**Figure S2A-C, S3, S4**, **Figure 1E**). The triple *mctp3-1/mctp4-1/mctp6-1* mutant was not viable when grown on soil and died after two weeks (**Figure S3)**. We next inquired about their interaction at the physical level. Using co-immunoprecipitation in transiently transformed *Nicotiana benthamiana* leaves, we first showed that MCTP3, MCTP4 and MCTP6 have indeed the potential to form hetero-oligomers when co-expressed (**Figure S2D**, **Figure 1F**). We confirmed this interaction at plasmodesmata in stable transgenic Arabidopsis plants using Förster Resonance Energy Transfer Fluorescence Lifetime Imaging Microscopy (FRET-FLIM) analysis with functional pMCTP4::TagRFP-MCTP4 co-expressed with pMCTP3::eYFP-MCTP3 in the complemented triple mutant background *mctp3-1/mctp4-1/mctp6-1* (**Figure 1G**). Altogether, these data indicate that 1) MCTP3, MCTP4 and MCTP6 interact at the physical and genetic level similar to E-Syts and SYTs, 2) at least two members need to be down regulated for phenotypic output with MCTP4 being a chief partner, and 3) loss-of-function high-order mutants result in a strong pleiotropic phenotype consistent with a role in the coordination of cellular activity at the multicellular level.

MCTPs act as ER/PM tether inside plasmodesmata bridges, controlling membrane contact

In previous work we showed that overexpression of MCTP4 in a delta-ER-PM tether yeast mutant could partially restore cortical ER, suggesting a potential function as membrane tether (Brault et al., 2019). To test whether MCTP3, MCTP4 and MCTP6 indeed act as ER-PM linkers inside plasmodesmata, we proceeded to investigate whether their genetic deletion would result in a loosening of the ER-PM gap within the bridges. As functional redundancy has been shown for E-Syts and SYTs (Saheki et al., 2016; Lee et al., 2020; Ruiz-Lopez et al., 2021) and only high order mutants show clear ER-PM detachment (Giordano et al., 2013), we focused on *mctp3-1/mctp4-1/mctp6-1* triple mutant and checked whether it presented defects in plasmodesmata structure. To test this hypothesis, we turned to the primary root, which allows high-resolution microscopy imaging of plasmodesmata nanoscopic structure by electron tomography on high-pressure frozen, freeze-substituted samples (Nicolas et al., 2017a; Yan et al., 2019). Electron tomography is the only imaging technology that can currently achieve the necessary resolution and accurately resolve 3D volumes at the nanometer scales relevant to plasmodesmata, that are no more than 20-30 nm in diameter (**Figure S5**). We focused on the root epidermis division zone, where plasmodesmata structure is well preserved after cryo-fixation, and on apical-basal walls where plasmodesmata are highly active in transport (Nicolas et al., 2017a). We adapted our previous protocol (Petit et al.; Nicolas et al., 2017a) to reduce staining and increase substructural resolution (see material and methods for details). This new protocol allowed us to visualize the ER-PM boundary within plasmodesmata and discern potential membrane detachment with more precision. Altogether we acquired over 60 tomograms of plasmodesmata. While in wild-type plants, a large proportion of plasmodesmata presented tight ER-PM contacts throughout the entire length of plasmodesmata (~63 % plasmodesmata; n=40) as previously described (Nicolas et al., 2017a) (**Figure 2A (i) and (ii), Movie S4),** this structural configuration was significantly diminished in the *mctp3-1/mctp4-1/mctp6-1* mutant (~7 % plasmodesmata; n=20). Instead, the majority of plasmodesmata in the *mctp3-1/mctp4-1/mctp6-1* mutant showed clear and visible ER-PM membrane detachment (~93% of plasmodesmata in *mctp3-1/mctp4-1/mctp6-1* mutant as opposed to ~27% in the wild-type) (**Figure 2A (i) and (ii), Movies S5-6**). In some cases (about ~10%), membrane separation in *mctp3-1/mctp4-1/mctp6-1* was nearly complete, as illustrated in **Figure 2A (i) (lower right panel)** (**Movie S6**), a configuration we never observed in the wild-type. Furthermore, when measuring the ER-PM distance at detachment points we observed larger values in the triple *mctp* mutant compared to wild-type (**Figure 2A (iii))**. These data indicate that MCTP3/MCTP4/MCTP6 act as ER-PM tethers inside the plasmodesmata bridges and that their loss-of-function leads to looser membrane junctions.

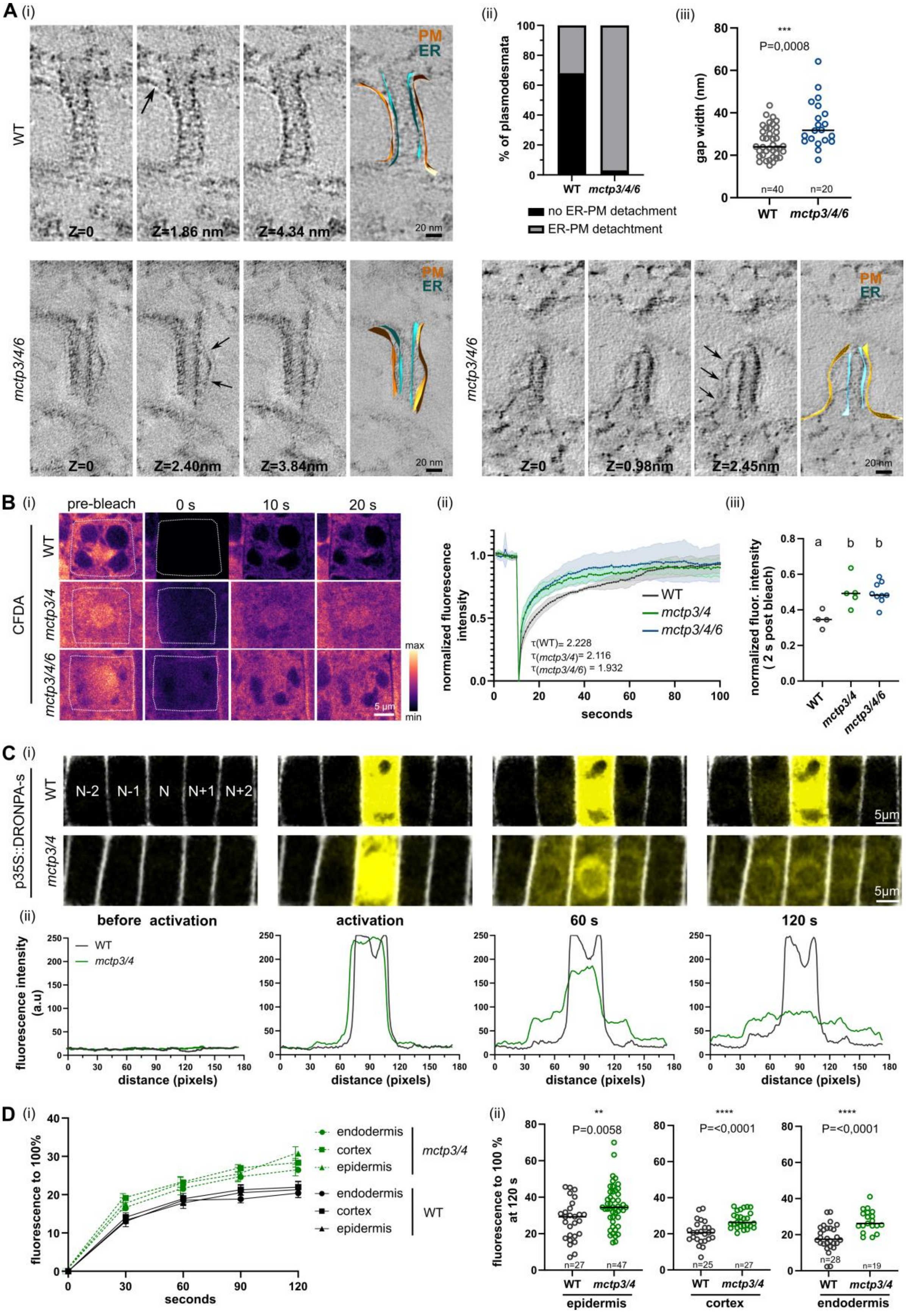
A (i)
WT
Z=0
Z=1.86 nm
Z=4.34 nm
PM
ER
20 nm
mctp3/4/6
Z=0
Z=2.40nm
Z=3.84nm
PM
ER
20 nm
mctp3/4/6
Z=0
Z=0.98nm
Z=2.45nm
PM
ER
20 nm
(ii)
% of plasmodesmata
100
80
60
40
20
0
WT
mctp3/4/6
no ER-PM detachment
ER-PM detachtment
(iii)
***
P=0,0008
gap width (nm)
80
60
40
20
0
n=40
n=20
WT
mctp3/4/6
B (i)
pre-bleach
0 s
10 s
20 s
CFDA
WT
mctp3/4
mctp3/4/6
max
min
5 µm
(ii)
normalized fluorescence intensity
1.0
0.5
0.0
0
20
40
60
80
100
seconds
WT
mctp3/4
mctp3/4/6
τ(WT)= 2.228
τ(mctp3/4)= 2.116
τ(mctp3/4/6) = 1.932
(iii)
normalized fluor. intensity (2 s post bleach)
0.8
0.6
0.4
0.2
0.0
a
b
b
WT
mctp3/4
mctp3/4/6
C (i)
p35S::DRONPA-s
WT
mctp3/4
N-2
N-1
N
N+1
N+2
5µm
5µm
(ii)
before activation
activation
60 s
120 s
fluorescence intensity (a.u)
250
200
150
100
50
0
WT
mctp3/4
0
30
60
90
120
150
180
distance (pixels)
D (i)
fluorescence to 100%
40
30
20
10
0
0
30
60
90
120
seconds
endodermis
cortex
epidermis
mctp3/4
endodermis
cortex
epidermis
WT
(ii)
fluorescence to 100 % at 120 s
80
60
40
20
0
**
P=0.0058
n=27
n=47
WT
mctp3/4
epidermis
****
P=<0,0001
n=25
n=27
WT
mctp3/4
cortex
****
P=<0,0001
n=28
n=19
WT
mctp3/4
endodermis

Figure 2. MCTPs regulate the ER-PM distance at plasmodesmata and cell-cell diffusion

(A) Measurement of ER-PM detachment through electron tomography. (i) Individual tomographic slices and segmented 3D reconstructions of plasmodesmata in WT and mctp3/4/6. Arrows pointing to ER-PM detachment. (ii). Contingency plot of the percentage of plasmodesmata showing ER-PM detachment. (iii). Quantification of the distance between ER and PM in WT and *mctp3/4/6* plasmodesmata at the point where the gap is the widest.
(B) CFDA mobility assay measured by FRAP in root epidermal meristematic cells in WT, *mctp3/4* and *mctp3/4/6*. A vertical rectangle containing 3 cells was bleached and fluorescence recovery was measured in the central cell. 4 to 9 roots were imaged per genotype and experiment. Experiment was repeated twice with similar results. (i). Representative images before and the indicated time after bleach (the cells used for quantification are surrounded by dotted squares). (ii). Normalized fluorescence intensity over a period of 90 seconds after bleaching. Half-life (τ) of CFDA recovery for each genotype is shown. (iii). Normalized fluorescence intensity 2 seconds after photobleaching. Statistical analysis was done with ANOVA followed by Tukey's test. Line shows median.
(C-D) DRONPA-s mobility assay measured as the diffusion of DRONPA-s signal from one single activated cell by two-photon into the neighboring cells in the longitudinal axis. At least 6 roots were used per cell type per genotype per experiment. Experiment was repeated 3 times and results were pooled for quantification. C (i). Representative images of the DRONPA-s signal in WT and *mctp3/4* before activation, at activation and 60 and 120 second post activation. N, activated cell; N±1, direct neighbors; N±2, second level neighbors. Propidium iodide (PI, white) was used to mark cell peripheries (ii). Signal plot showing raw intensity values from the images in (i). D (i). Normalized fluorescence over time of DRONPA-s averaged from N±1 in meristematic epidermis, cortex and endodermis cells imaged every 15 seconds. Bars show SEM. (ii). Mean percentage of DRONPA-s normalized fluorescence in the N±1 cells at 120 seconds post activation from (ii). Statistical analysis was done with Student t-text. Line shows median.

Loss of MCTP ER-PM tethers increases intercellular molecular flow through plasmodesmata

We next tested the impact of ER-PM membrane detachment and change in plasmodesmata structure on intercellular trafficking in the MCTPs loss-of-function mutants. We first used fluorescence recovery after photobleaching (FRAP) on the carboxyfluorescein diacetate (CFDA) cytosolic dye. CFDA is a cell-permeant compound which once loaded in the cells is cleaved by intracellular esterases, creating a membrane-impermeable fluorescent probe that moves from cell to cell through plasmodesmata (Nicolas et al., 2017a). After photobleaching in the root division zone, we noted a significantly faster recovery in both *mctp3-2/mctp4-1* and *mctp3-1/mctp4-1/mctp6-1* mutants compared to wild type (**Figure 2B**). No differences were noted in terms of recovery rate between the *mctp3-2/mctp4-1* and *mctp3-1/mctp4-1/mctp6-1* mutants. This can be attributed to the previous finding that MCTP6 is downregulated at the protein level in the *mctp3-2/mctp4-1* mutant background (Brault et al., 2019).

To validate that the relaxation of ER-PM contacts within plasmodesmata is indeed leading to an increase in molecular flow, we next employed the genetically encoded DRONPA-s, a reversibly switchable photoactivatable fluorescent marker. DRONPA-s is much bigger than CFDA with an estimated Stoke radius of 2.8 nm against only 0.61 nm for CFDA, allowing us to assess how molecules of different sizes behave. Cytosolic DRONPA-s can be selectively activated in a single cell through two-photon excitation microscopy, and movement into neighboring cells can be monitored over time to assess plasmodesmata molecular flow capacity (Gerlitz et al., 2018). This approach enabled us to precisely evaluate variations in transport within the apico-basal walls of the root epidermis division zone, where the tomography study was conducted. We selected both the double *mctp3-2/mctp4-1* and the triple *mctp3-1/mctp4-1/mctp6-1* mutants to express cytosolic DRONPA-s. However, and despite repetitive attempts, we only obtained sufficient DRONPA-s expression levels in the double *mctp3-2/mctp4-1* mutant. After activation of DRONPA-s in one cell (N), its cell-cell transport can be monitored as the loss of DRONPA signal in the activated cell or the gain of DRONPA-s in the neighbors (N+1, N+2 and N-1, N-2) over time (**Figure 2C-D**).

Loss-of-function in *mctp3-2/mctp4-1* resulted in much faster DRONPA-s loss in the activated cell and significantly increased movement in the N±1 neighboring cells (**Figure 2C-D**; **Movie S7**), indicating that plasmodesmata efflux capacity was more permissive than in wild-type plants. To ensure that the increased molecular flow was not specific to a particular cell type, we also evaluated transport capacity in both the endodermis and cortex. Both cell layers presented a similar increase in cell-cell trafficking capacity in the double *mctp3-2 mctp4-1* mutant as compared to the wild-type (**Figure 2D**). Together these data show that modifying the ER-PM contacts by means of MCTP3/MCTP4/MCTP6 tether complex, modifies plasmodesmata transport capacity.

Heightened cell-to-cell diffusion in *mctp* mutants is independent of callose deposition

In the text-book model, plasmodesmata cell-cell trafficking is primarily regulated by callose, a beta 1-3 extracellular glucan, that is specifically enriched around plasmodesmata and metabolized by plasmodesmata-located enzymes. Functionally, callose accumulation reduces cell-cell transport while degradation increases transport (Amsbury et al., 2017). Although callose mode of action remains elusive, it has been proposed to act by increasing or relaxing pressure on the PM, thereby modulating the size of the cytoplasmic sleeve. We therefore enquired if the increase of cell-cell molecular transport in *mctp3-2/mctp4-1* and *mctp3-1/mctp4-1/mctp6-1* mutants was due to a downregulation of callose levels. We first checked if the expression of plasmodesmata associated callose-modulating genes was modified in our *mctp* mutants. For that we performed RNAseq analyses on root extracts from wild type, *mctp3-2*, *mctp4-1* and *mctp3-2/mctp4-1*. Our data indicate that none of the callose-relevant proteins were mis-regulated in either the single *mctp3-2* or *mctp4-1* mutants, or in the *mctp3-2/mctp4-1* double mutant when compared to wild-type plants (**Figure 3A; Figure S6**). Callose levels at plasmodesmata can also be adjusted through post-transcriptional modification. We therefore directly quantified callose levels *in situ* in the root division zone by whole-mount immunolocalization using callose-specific monoclonal antibody, in the same area used for DRONPA-s cell-cell trafficking assay (**Figure 3B)**. The immunostaining revealed that *mctp* mutants presented the same endogenous accumulation of callose as wild-type plants, whatever the cell layer considered (**Figure 3 C**). From these data we concluded that the increase of cell-cell trafficking in *mctp* mutants is not caused by a reduction of callose levels.

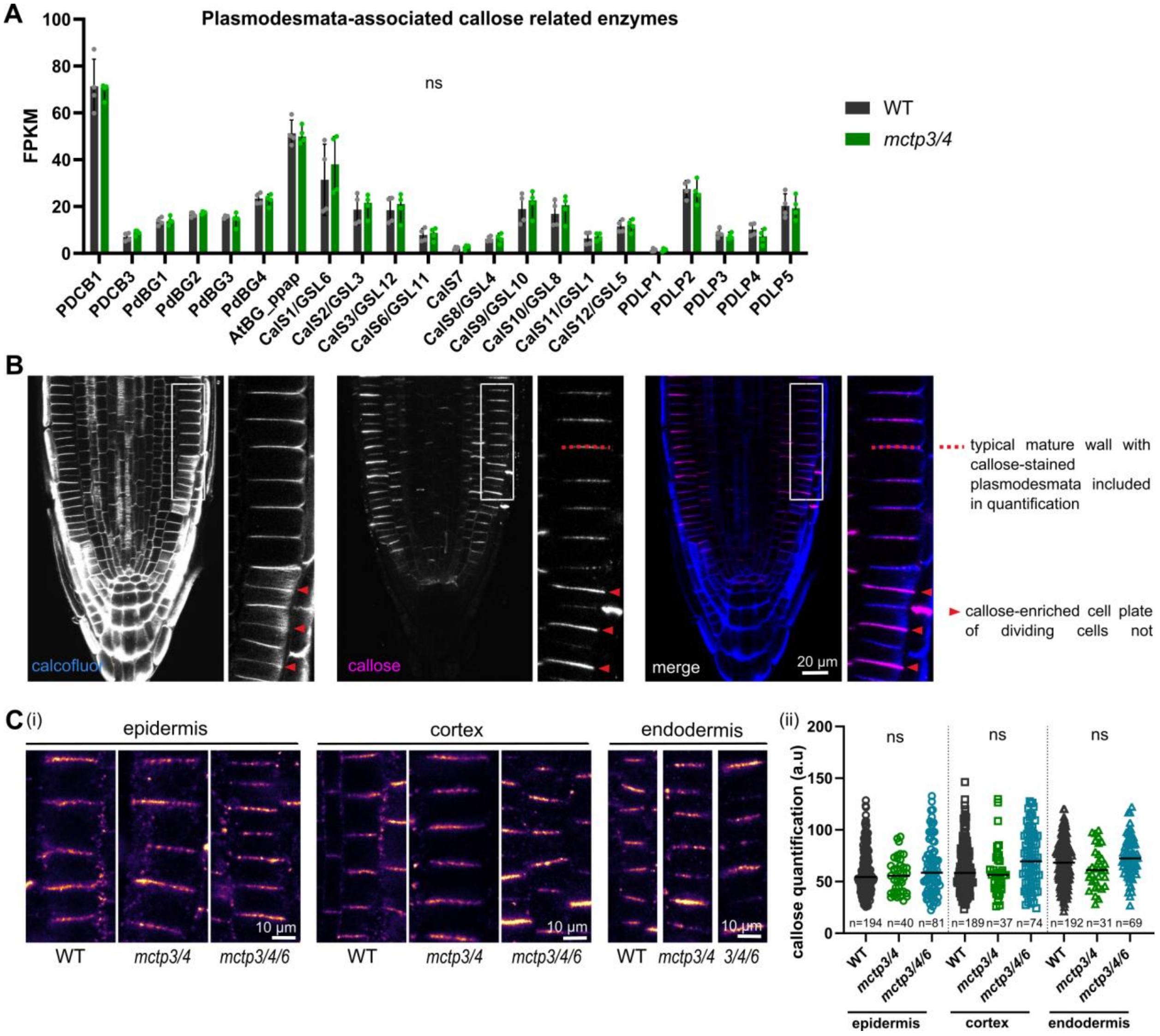

Figure 3. Loss of function of MCTP does not induce defects in callose deposition

(A) Normalized expression of callose related enzymes based on mRNA-seq from WT and *mctp3/4*. Statistical analysis was done with multiple paired t-test. FPKM, Fragments per kilobase mapped. Bars reach the value of the median, error bars represent 95 % CI. Experiment includes 4 biological replicates, each of them being a pool of 0.4 mg of 5 days old roots cut at 1 cm from the tip.

(B) Representative images of whole-mount anti-callose immunostaning (magenta) of WT showing the root apical meristem. Calcofluor-white (blue) was used to stain cell-walls. The white rectangle indicates the area generally used for quantification. For each mature cell-wall, a segmented line was drawn (dashed-red line as an example) and the mean intensity value along the line was used for quantification. Red arrowheads point to cell-walls that are not included in the analysis because they are just formed, as indicated by a very intense anti-callose signal and weak calcofluor-white signal.

(C) Callose accumulation in the epidermis, cortex and endodermis meristematic cells of WT, *mctp3/4* and *mctp3/4/6*. (i). Representative confocal images of anti-callose immunostaining. (ii). Quantification of callose as explained in B. Statistical analysis was done with ANOVA followed by Tukey's test. Line indicates median. A minimum of 4 roots were used per genotype, per experiment. Experiment was repeated two times with similar results and data were pooled together.

Defective ER-PM tethering impairs the dynamic control of intercellular molecular flow

Intercellular communication is dynamically controlled and a key feature of plasmodesmata lies in their ability to respond to various environmental or developmental stimuli by reducing or increasing intercellular molecular flow (Gisel et al., 1999; Faulkner et al., 2013; Han et al., 2014; Cui and Lee, 2016; Cheval and Faulkner, 2018; Gaudioso-Pedraza et al., 2018; Lexy et al., 2018; Tylewicz et al., 2018; Grison et al., 2019; Sager et al., 2020; Mehra et al., 2022; Tee et al., 2022; Wang et al., 2023). We therefore tested whether dynamic regulation of trafficking persisted in the absence of a fully functional tether machinery.

First, we investigated if the down-regulation of cell-cell trafficking was still functional in the absence of MCTP tethers. To address this, we tested the response of *mctp* mutants in two conditions known to induce plasmodesmata closure. To start with, we examined plasmodesmata response to brassinosteroid levels, a hormone that modifies cell-cell transport and callose deposition at plasmodesmata as we recently reported (Wang et al., 2023). As expected, in wild-type plants exposed to brassinolide (24h, 200 nM), the most bioactive brassinosteroid, we observed the closure of plasmodesmata, as evidenced by a reduction in DRONPA-s cell-cell diffusion in the root epidermis (**Figure 4A**), and increased callose accumulation (**Figure 4B**). Under the same condition, *mctp* mutants showed callose accumulation levels identical to those of wild-type plants (**Figure 4B**). However, the impact on cell-cell trafficking was minor and DRONPA-s diffusion remained to the same permissive level in brassinolide-treated *mctp4-1/mctp3-2* mutant than in mock-treated wild type plants (**Figure 4A**).

We next turned to a more rapid trigger considering that a long-term 24h treatment may provide plants with more time to activate compensatory mechanisms, thereby partially masking MCS contribution in regulating cell-cell trafficking. We used salt stress (15 min, 20 mM), which triggers short-term callose deposition and plasmodesmata closure (Hunter et al., 2019), as confirmed by quantitative callose immunolocalization and DRONPA-s diffusion (**Figure 4C-D**). Again, callose deposition was induced to a similar extent in *mctp3-2/mctp4-1* or *mctp3-2/mctp4-1/mctp6-1* mutants as in wild-type roots (**Figure 4D**). However, under short-term salt stress, plasmodesmata closure was barely observable in *mctp3-2/mctp4-1* mutants, while in wild-type, a strong decrease in DRONPA-s diffusion was measured (**Figure 4C**). These data indicate that in the absence of MCTP tethers, dynamic down-regulation of molecular flow is less effective and can even be compromised.

We next questioned how callose removal in the *mctp* mutant would impact molecular flow, whether it would lead to an additive effect, resulting in even greater molecular flow, or not. We manipulated callose levels to lower them to a minimum using brassinazole, a brassinosteroid biosynthesis inhibitor which drastically reduces callose levels at plasmodesmata in Arabidopsis roots (Wang et al., 2023). Upon exposure to brassinazole (24h, 1 µM), wild-type roots exhibited almost complete suppression of callose accumulation at plasmodesmata (**Figure 4F**). This effect was similarly observed in both *mctp3-2/mctp4-1* and *mctp3-1/mctp4-1/mctp6-1* mutants, reaffirming that the callose response remains unaffected in the *mctp* mutants (**Figure 4F**). As anticipated, in wild-type plants, DRONPA-s exhibited a faster spread into neighboring cells after the nearly complete elimination of callose (**Figure 4E**). In this condition, cell-cell trafficking in wild-type increased to the same magnitude as in untreated *mctp3-2/mctp4-1* mutant (so with control callose levels). Meanwhile, callose removal in the *mctp3-2/mctp4-1* mutant did not change macromolecular flux, which remains identical to control conditions (**Figure 4E**).

Altogether, these data indicate that 1) effective regulation of cell-cell molecular flow is lost in *mctp* mutants 2) callose action is less effective in the absence of functional ER-PM tethers (*i.e.* callose accumulation does not effectively close plasmodesmata, whereas removing callose fails to open them more), suggesting that the modification of ER-PM tethering may have a dominant function over callose.

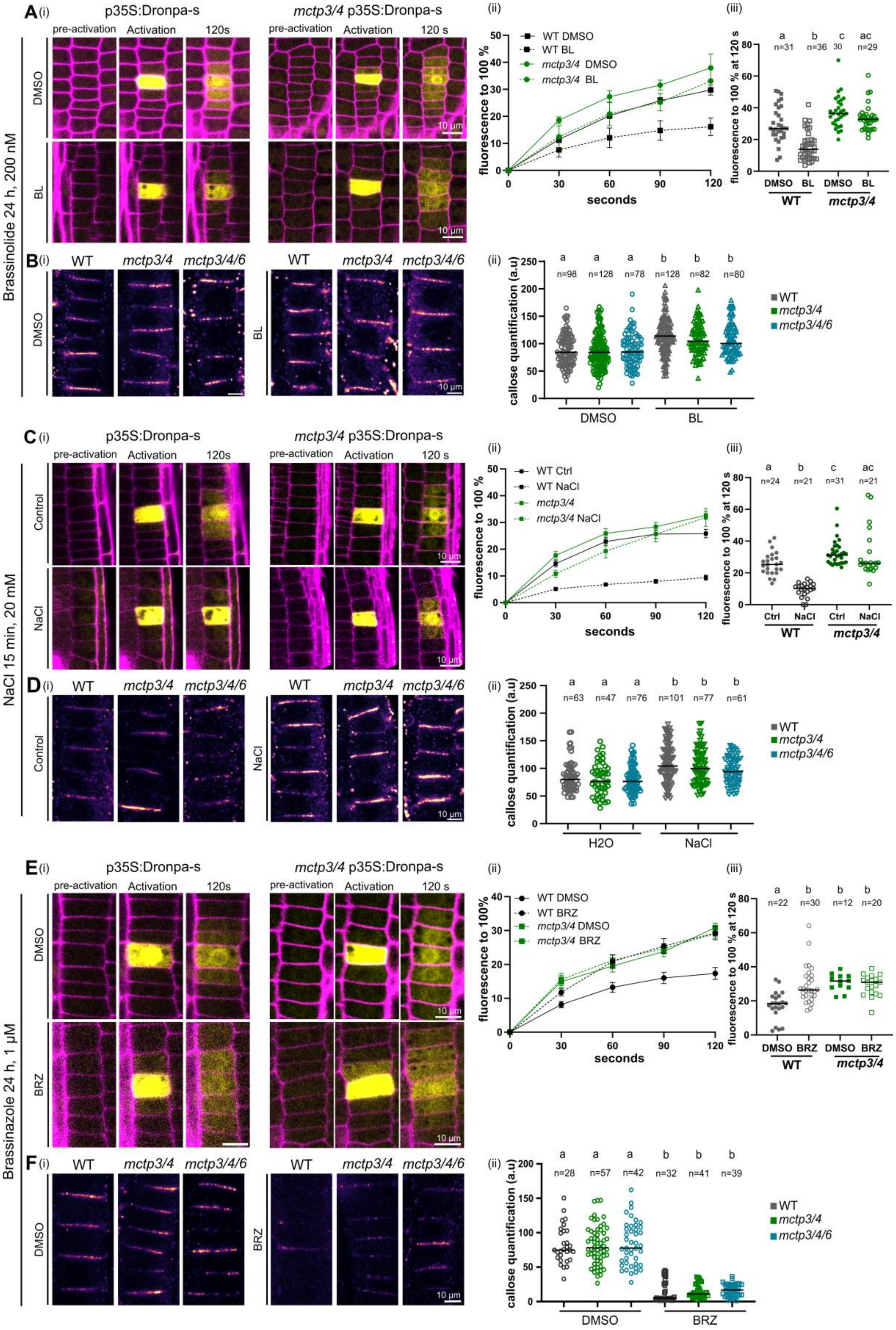
A (i)
p35S:Dronpa-s
mctp3/4 p35S:Dronpa-s
pre-activation
Activation
120s
120 s
DMSO
BL
10 µm
Brassinolide 24 h, 200 nM
(ii)
WT DMSO
WT BL
mctp3/4 DMSO
mctp3/4 BL
fluorescence to 100 %
seconds
0
30
60
90
120
(iii)
fluorescence to 100 % at 120 s
a b c ac
n=31 n=36 30 n=29
DMSO BL DMSO BL
WT
mctp3/4
B (i)
WT
mctp3/4
mctp3/4/6
DMSO
BL
10 µm
(ii)
callose quantification (a.u)
a a a b b b
n=98 n=128 n=78 n=128 n=82 n=80
DMSO
BL
WT
mctp3/4
mctp3/4/6
C (i)
p35S:Dronpa-s
mctp3/4 p35S:Dronpa-s
pre-activation
Activation
120s
120 s
Control
NaCl
10 µm
NaCl 15 min, 20 mM
(ii)
WT Ctrl
WT NaCl
mctp3/4
mctp3/4 NaCl
fluorescence to 100 %
seconds
(iii)
fluorescence to 100 % at 120 s
a b c ac
n=24 n=21 n=31 n=21
Ctrl NaCl Ctrl NaCl
WT
mctp3/4
D (i)
WT
mctp3/4
mctp3/4/6
Control
NaCl
10 µm
(ii)
callose quantification (a.u)
a a a b b b
n=63 n=47 n=76 n=101 n=77 n=61
H2O
NaCl
WT
mctp3/4
mctp3/4/6
E (i)
p35S:Dronpa-s
mctp3/4 p35S:Dronpa-s
pre-activation
Activation
120s
120 s
DMSO
BRZ
10 µm
Brassinazole 24 h, 1 µM
(ii)
WT DMSO
WT BRZ
mctp3/4 DMSO
mctp3/4 BRZ
fluorescence to 100%
seconds
(iii)
fluorescence to 100 % at 120 s
a b b b
n=22 n=30 n=12 n=20
DMSO BRZ DMSO BRZ
WT
mctp3/4
F (i)
WT
mctp3/4
mctp3/4/6
DMSO
BRZ
10 µm
(ii)
callose quantification (a.u)
a a a b b b
n=28 n=57 n=42 n=32 n=41 n=39
DMSO
BRZ
WT
mctp3/4
mctp3/4/6

Figure 4. Callose regulation in loss of function MCTPs has minor effects on the cell-cell diffusion

(A-B) Brassinolide treatment. (A) DRONPA-s mobility assay in WT and *mctp3/4* treated with DMSO or 200 nm Brassinolide (BL) for 24 h. (i). Representative confocal images before activation, at activation or 120 s after two-photon activation in a single cell. (ii). Normalized fluorescence over time of DRONPA-s averaged from N±1 imaged every 15 s. Bars show SEM. (iii). Mean percentage of DRONPA-s normalized fluorescence in the N±1 cells at 120 s post activation from (ii). (B) Anti-callose immunostaining in WT, *mctp3/4* and *mctp3/4/6* treated with DMSO or 200 nm BL for 24 h. (i). Representative confocal images of callose immunostaining. (ii). Quantification of callose.

(C-D) Salt short-term treatment. (C) DRONPA-s mobility assay in WT and *mctp3/4* treated with H2O (control) or 20 mM NaCl for 15 min. (i). Representative images of DRONPA-s diffusion. (ii). Normalized DONRPA-s fluorescence over time. Bars show SEM. (iii). Mean percentage of DRONPA-s normalized fluorescence in the N±1 cells at 120 s post activation from (ii). (D) Anti-callose immunostaining in WT, *mctp3/4* and *4* and *mctp3/4/6* treated with H2O (control) or 20 mM NaCl for 15 min. (i). Representative confocal images of callose immunostaining. (ii). Quantification of callose.

(E-F) Brassinazole treatment. (E) DRONPA-s mobility assay in WT and *mctp3/4* treated with DMSO or 1 µM Brassinazole (BRZ) for 24 h. (i). Representative images of DRONPA-s diffusion. (ii). Normalized DONRPA-s fluorescence over time. Bars show SEM. (iii). Mean percentage of DRONPA-s normalized fluorescence in the N±1 cells at 120 s post activation from (ii). (F) Anti-callose immunostaining in WT, *mctp3/4* and *mctp3/4/6* treated with DMSO or 1 µM BRZ for 24 h. (i). Representative confocal images of callose immunostaining. (ii). Quantification of callose.

When not specified differently, line indicates median. Statistical analysis was done with ANOVA followed by Tukey's test. Minimum of 5 roots were used per genotype, per condition, per experiment. Experiments were repeated three times with similar results and data were pooled together.

MCS regulates cell-cell molecular flow through the tandem action of MCTP tethers and PI4P lipid.

MCTPs are anchored into the ER through their C-terminal transmembrane region, and were proposed to dock to the PM by interacting with anionic lipids through their C2-lipid binding domains (Brault et al., 2019) akin to E-Syts and SYTs (Giordano et al., 2013; Pérez-Sancho et al., 2015; Benavente et al., 2021) **(Movie S8**). We therefore wondered if anionic lipids could regulate plasmodesmata, by controlling the binding between the ER and the PM, thereby influencing the flow of molecules between cells.

We focus on PI4P, which was previously identified as a prime determinant of the PM inner leaflet electrostatic signature in plants (Simon et al., 2016a). Earliest studies on individual MCTP C2 domains previously suggested that PI4P may indeed promote docking to the PM. To confirm these data, we purified individual C2 domains of the master regulator MCTP4. While C2C and C2D were insoluble after expression in bacteria, we managed to purify soluble C2B. We then performed liposome sedimentation assays with liposomes of different lipidic composition and confirmed preferential binding of MCTP4-C2B to the lipid bilayer in the presence of PI4P (**Figure 5A**). While PI4P is known to be present at the bulk PM, plasmodesmata, as any MCS, display a specialized membrane environment (Li et al., 2021) and it is not known whether they contain phosphoinositide species. We thus purified plasmodesmata from *A. thaliana* cell culture as in (Brault et al., 2019) and ran LC-MS/MS analysis. Both PIP and PIP2 species were indeed detected in plasmodesmata fractions (**Figure 5B**). Thus, MCTP tethers can interact with PI4P, an anionic lipid specie present at plasmodesmata.

Having confirmed the presence of phosphoinositides at plasmodesmata, we next tested the impact of PI4P on cell-cell trafficking. Our data supports a scenario where MCTPs bind to the PM through interaction with PI4P and the removal of PI4P should phenocopy *mctp3-2/mctp4-1* in terms of cell-cell transport capacity. To test this hypothesis, we first assessed the effect of reduced PI4P levels by applying the PI4K inhibitor PAO (phenylarsine oxide) at a concentration and exposure time previously described to affect the localization of PI4P sensors in Arabidopsis roots (Simon et al., 2016a) (**Figure 5C**). We then subjected PAO-treated wild-type plants expressing cytosolic DRONPA-s to our cell-cell connectivity test. The data showed that inhibiting PI4P synthesis in wild-type plants increases cell-cell trafficking to a similar level than in the non-treated *mctp3-2/mctp4-1* mutant (**Figure 5C**). By contrast, using YM201636 (an inhibitor of PI(3,5)P_2 synthesis) or low concentration of Wortmannin (an inhibitor of PI3P synthesis) did not change the cell-cell trafficking properties of plasmodesmata (**Figure S7A-C**). We then subjected *mctp3-2/mctp4-1 p*35S::DRONPA-s to the same PAO treatment. The mutant transport capacity was not affected by PAO (**Figure 5C**), consistent with the notion that MCTP and PI4P act together to tether the ER to the PM at plasmodesmata. We also checked that neither PAO nor DMSO affected callose levels in wild-type and *mctp3-2/mctp4-1* mutant backgrounds (**Figure S7D**).

If PI4P levels are indeed instrumental to the regulation of cell-cell trafficking, elevated PI4P should result in plasmodesmata closure. Therefore, we next assayed if an increased PI4P level modifies DRONPA-s cell-cell diffusion. To do so, we generated a stable line expressing DRONPA-s in the *suppressor of actin7* (*sac7*, also known as *root hair defective4*) mutant. SAC7 is a PI4P 4-phosphatase, whose mutant accumulates PI4P *in vivo* (Song et al., 2021). The data showed that the *sac7* mutant presents reduced cell-to-cell diffusion of DRONPA-s, strengthening the contribution of PI4P in controlling plasmodesmata connectivity (**Figure 5D**). Lastly, we quantified the callose levels in *sac7*. Compared to the wild-type, the mutant has decreased accumulation of callose, thus ruling out callose as the cause of plasmodesmata closure **(Figure S7E**). Altogether, we found that the signaling lipid PI4P can control cell-to-cell cytoplasmic diffusion, with reduced PI4P levels enhancing molecular movement, and elevated PI4P levels diminishing molecular flow.

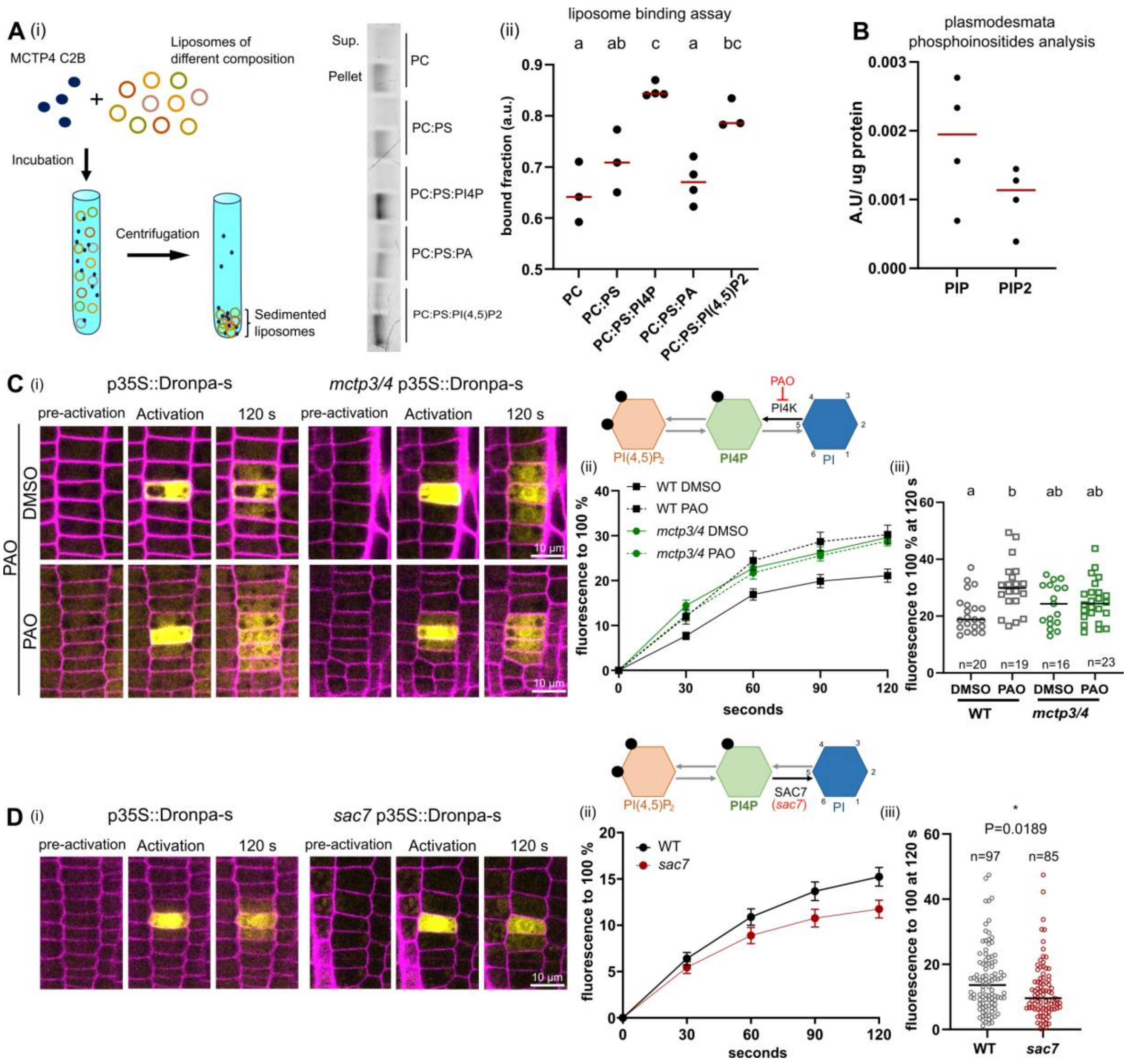

Figure 5. MCTP interacts with PI4P to regulate cell-cell diffusion

(A) Liposome binding of the purified C2B domain of MCTP4. (i). Schematic representation of the liposome binding assay. Different colors indicate liposomes of different composition. (ii). SDS-PAGE of the supernant (sup.) and precipitated (pellet) fractions after centrifugation. Proteins were visualized with a Bio-Rad stain-free imager and one single band was observed in each well, corresponding to the C2B domain of MCTP4. (iii). Quantification of the binding of C2B domain of MCTP4 to liposomes of different lipid compositions. Bound fraction was calculated as the ratio between C2B in the pellet and C2B in the supernatant. Line indicates median. Statistical analysis was done using ANOVA followed by Tukey test. Experiment was repeated 3-4 times and data were pooled together.

(B) Identification of phosphoinositides in plasmodesmata purified from WT cell cultures. Experiment includes 4 biological replicates.

(C) DRONPA-s diffusion assay in WT and *mctp3/4* treated with DMSO or PAO 60 nM for 30 min. (i). Representative images of DRONPA-s diffusion. (ii). Normalized DONRPA-s fluorescence over time. Bars show SEM. (iii). Mean percentage of DRONPA-s normalized fluorescence in the N±1 cells at 120 seconds post activation from (ii). Statistical analysis was done using ANOVA followed by Tukey's test. Line indicates median. A minimum of 5 plants per genotype, per condition, per experiment were used. Experiment was repeated 3 times and data were pooled together.

(D) DRONPA-s diffusion assay in WT and *sac7* meristematic epidermal cells. (i). Representative images of DRONPA-s diffusion. (ii). Normalized DONRPA-s fluorescence over time. Bars show SEM. (iii). Mean percentage of DRONPA-s normalized fluorescence in the N±1 cells at 120 seconds post activation from (ii). Statistical analysis was done using Student t-test. Line indicates median. A minimum of 20 roots per genotype, per experiment were used. Experiment was repeated 3 times and data were pooled together. C(ii) and D(ii). Error bars show standard SEM.

We next addressed the molecular mechanisms underlying PI4P's role in relation to MCTP membrane tethering activity. We turned to molecular modelling and molecular dynamics to obtain near-atomistic structural and energetic insights into MCTP4's interaction with the PM, with spatio-temporal resolution. In previous work we only assessed individual C2 domains (Brault et al., 2019), here we investigated the behavior of the entire MCTP4 cytosolic domain (the full protein but without the C-terminal ER-anchored transmembrane region) in the presence of a PM-like lipid bilayer. We conducted molecular dynamics simulations using the recently introduced Martini 3 coarse-grained force field (Souza et al., 2021; Borges-Araújo et al., 2023) and we employed Alphafold for protein structure prediction (Jumper et al., 2021). MCTPs are anchored into the ER via their TMR domain, restricting their 3D orientation relative to the PM plane. In order to focus solely on functionally relevant protein positioning, we restricted movement in the MCTP4 C2 cytosolic domain, ensuring that the TMR did not orient toward the PM (**Figure 6A**). The structural model for the cytoplasmic part of MCTP4, comprising the three C2 domains, was extracted from Sritharan et al. (Sritharan et al., 2023) and embedded in a water box with a lipid bilayer mimicking the PM composition, (~70% phosphatidylcholine (PC), 20% Sitosterol, 10% phosphatidylserine (PS)) but with varying concentration of PI4P (0%, 2%, 6%). To check the interactions between MCTP4 and the PM, we analyzed the fluctuating distances between the C2 domains and the lipid bilayer over time **(Figure 6B)** and the distribution of distances as a function of sequence (y axis) and time (x axis) (**Figure 6C).** The data indicate that PI4P boosts the frequency of binding between the C2 domains and the PM, implying a role in stabilizing PM docking (**Figure 6D**). Interactions with the PM involve multiple docking configurations, wherein combinations of C2/membrane interaction patterns differ, involving either one C2 (C2C **Figure 6E state3** or C2D **Figure 6E state4**), two C2s (C2B and C2C) **(Figure 6E state1)**, or all three **(Figure 6E state2)**.

From these data we concluded that 1) PI4P acts as a regulator of plasmodesmata connectivity. Low PI4P accumulation results in plasmodesmata opening, while high PI4P levels lead to plasmodesmata closure. 2) The levels of PI4P directly influence MCTP-membrane docking presumably regulating ER-PM spacing hence plasmodesmata connectivity.

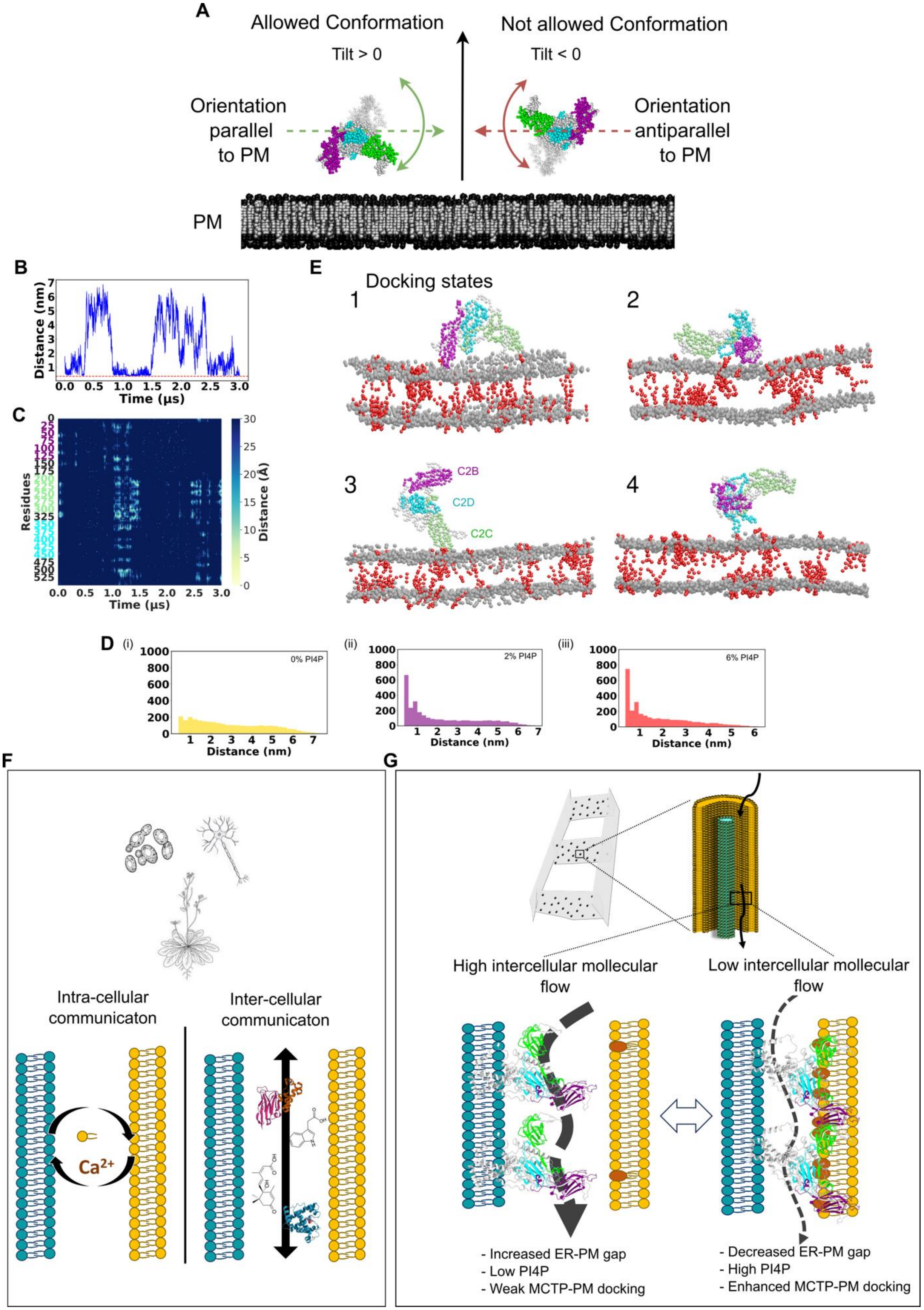
A
Allowed Conformation
Tilt > 0
Orientation parallel to PM
Not allowed Conformation
Tilt < 0
Orientation antiparallel to PM
PM
B
Distance (nm)
Time (μs)
C
Residues
Distance (Å)
Time (μs)
D
(i) 0% PI4P
(ii) 2% PI4P
(iii) 6% PI4P
Distance (nm)
E
Docking states
1
2
3
4
C2B
C2D
C2C
F
Intra-cellular communicaton
Inter-cellular communicaton
Ca2+
G
High intercellular mollecular flow
Low intercellular mollecular flow
- Increased ER-PM gap
- Low PI4P
- Weak MCTP-PM docking
- Decreased ER-PM gap
- High PI4P
- Enhanced MCTP-PM docking

Figure 6. PI(4)P regulates the docking of MCTP4 to the PM by interacting with C2-lipid binding domains
(A) Application of the Colvar Tilt variable to the MCTP4. The harmonic potential activates when the tilt angle is below 0, constraining the system to maintain a realistic orientation relative to the membrane in the absence of the TMR/ER.
(B) Analysis of the minimum distance between the C2 domains and the lipid bilayer over 3 microseconds, illustrating the dynamics of domain-membrane interactions.
(C) Heatmap visualization representing the distances between C2 domain residues and PI4P in the membrane, indicating interactions with PI4P.
(D) Histograms comparing the interaction frequency under three PI4P conditions: without PI4P, with 2% PI4P, and with 6% PI4P, showing increased frequency and stabilization of MCTP4-PM interactions correlating with higher PI4P concentrations. The distances are color coded according to the legend in the right.
(E) Snapshots from a simulation of the MCTP4 cytoplasmic domain engaging with a PM-like lipid bilayer in the presence of 2% PI4P: (1) Interaction through two C2 domains, (2) All three C2 domains simultaneously interacting with the bilayer, and (3 & 4) interaction with one different C2 domain.
The simulations lasted 3 microseconds and were repeated 5 times for each condition. The 2 C2 domains appear in different colors: C2B, magenta; C2C, green; C2D, cyan.
(F) MCS function spans from inter-organelle to inter-cellular function in eucaryotes.
(G) Dynamic regulation of plasmodesmata MCS and its impact on molecular traffic.

Discussion

Our results uncover two important findings. Firstly, we reveal that while MCS are typically linked to inter-organellar communication in eukaryotes, they can also operate at cell-cell interface to govern inter-cellular communication. Plasmodesmata bridges, prevalent across the Plantae kingdom, function as unconventional tubular ER-PM MCS managing direct molecular exchange between neighboring cells. Similar to other MCS, the regulation of membrane contacts at plasmodesmata involves a complex molecular partnership consisting of phosphoinositides and protein tethers. However, in contrast to the typical MCSs, which primarily govern direct molecular exchange between the organelles in contact, plasmodesmata MCS serve to control the flow of molecules between adjacent cells (**Figure 6F**). To our knowledge, this marks the initial discovery of the functional involvement of MCS in direct intercellular exchange and hints at a new conceptual framework. Recent findings support the notion that MCS may also function in cell-cell communication in animals. A recent preprint reports two ER-PM MCS-associated proteins, TMEM24 and C2CD2, to be involved into cell-cell contact interaction in neurons (Johnson et al., 2023), although experimental support for effective communication is still lacking. Likewise, Bharathan et al. described close contact between the ER and desmosomal intercellular junctions (Bharathan et al., 2023). This work has sparked inquiries into whether an integrated ER-keratin-desmosome contact zone could facilitate the transmission of ER stress signals between cells. Our study brings this concept one step further and demonstrates the functional involvement of multicellular eucaryotic MCS in direct intercellular exchanges.

The second significant discovery in this study is that it questions the prevailing textbook model concerning the regulation of plasmodesmata-mediated cell-cell trafficking. Unquestionably, callose, a beta 1-3 glucan that undergoes both degradation and synthesis around plasmodesmata, is presently acknowledged as the primary gate keeper of plasmodesmata. Numerous studies report the involvement of callose in opening or closing plasmodesmata in a wide range of developmental and physiological responses. The prevailing concept behind callose action is that callose build-up would create pressure on the PM, causing it to push against the ER, therefore obstructing cellular traffic by reducing the size of the cytoplasmic sleeve. However, recent research in the field suggests that callose actually functions as a plasticizer, enhancing wall flexibility, rather than forming a rigid donut-shaped structure that presses against the PM (Abou-Saleh et al., 2018). Moreover, extreme proximity between the ER and PM, which can be as little as 3-4 nm (Nicolas et al., 2017a), is likely to require membrane bridging-complexes to induce and to stabilize the contact. In this work we show that without the molecular machinery acting at the ER-PM interface (*i.e.* PI4P and MCTP tethers) dynamic regulation of plasmodesmata is compromised even if callose regulation is still functional. In the absence of the MCTP tethers, the precise control of molecular flow through plasmodesmata is lost, regardless of whether callose levels are upregulated or downregulated. When callose deposition is triggered in the *mctp* mutant, through NaCl or brassinolide treatments, plasmodesmata fail to accurately reduce molecular flow. Conversely, when callose levels are significantly diminished through treatment with brassinazole, plasmodesmata are unable to open further. In the same line, an increase in PI4P levels in a *sac7* mutant reduces cell-cell trafficking, while reducing PI4P levels increase cell-cell trafficking, which we attribute to enhanced or reduced MCTP-docking to the PM, as supported by liposome binding and molecular dynamics. Collectively our data indicate that MCTP/PI4P serve as primary controllers of plasmodesmata opening and closing, working independently of callose. This finding introduces a new perspective on how intercellular molecular flow is regulated in plants, and opens the door to a more intricate regulatory mechanism than previously thought.

How could MCTP/PI4P dynamically regulate molecular flow across plasmodesmata MCS? The most straightforward hypothesis is by modulating the ER-PM gap (**Figure 6G**). Theoretical models suggest that changes in plasmodesmata structure directly affect the rate of molecular flow through these channels (Deinum et al., 2019; Ostermeyer et al., 2022). This is notably influenced by the internal geometry and size of the cytoplasmic sleeve (defined as the space between the two membranes), which determines the resistance to diffusion or convective flow. The MCTP family comprises 16 members in Arabidopsis, and the deletion of three members, specifically MCTP3, MCTP4, and MCTP6, leads to a noticeable alteration in ER-PM tethering within plasmodesmata. This structural modification is associated with an increase in the global molecular flow between adjacent cells. This rise in cell-cell trafficking occurs in a context where loss-of-function mutants for *mctp3/mctp4* and *mctp3/mctp4/mctp6* exhibit a significant reduction of approximately 30% to nearly 50% in the number of plasmodesmata in the root meristem (Li et al., 2023). This suggests that the transport capacity of a single plasmodesma is considerably greater in *mctp* mutant background compared to wild-type.

What are the underlying molecular mechanisms responsible for regulating the ER-PM gap? Conditional docking of MCTPs to the PM, conformational changes, oligomerization or dynamic recruitment of MCTP tethers within plasmodesmata all have the potential to regulate ER-PM spacing and thus intercellular trafficking. Our data also indicate that MCTPs operate in coordination with the anionic lipid PI4P. We show that MCTP4, which based on genetic evidence serves as a central element of the MCTP3/MCTP4/MCTP6 complex, establishes a direct interaction with PI4P through its C2 domains as indicated by liposome binding assays and molecular dynamics. Furthermore, molecular dynamics simulations suggest that the levels of PI4P directly influence MCTP's attachment to the PM. This model is corroborated by the experimental finding that when PI4P production is up- or down-regulated, cell-cell transport is either hindered or facilitated. How could cells potentially modify PI4P levels to regulate cell-cell transport capacity? This could occur through the action of PI4P-related enzymes like PI4P kinases or SAC7, which quickly adjust membrane-localized substrates of PI or PI4P to manage PI4P levels (either increase or decrease). Increase of PI4P would then favor MCTP docking to the PM hence ER-PM close contact. The system however does not operate with a binary on/off mode; instead, MCTP docking simply becomes more frequent in the presence of PI4P, and this frequency escalates with higher PI4P concentrations. Note that these effects may also act in a tissue-specific manner (Brault et al., 2019). Upcoming research will focus on delving deeper into how MCTP/phosphoinositide interplay dynamically regulates intercellular communication and their roles in plant development and environmental responses.

Acknowledgments: We would like to thank Paulo Telles de Souza for sharing Martini3 coarse grain parameter for sitosterol**.** Fabrice Cordelières for live-imaging data display. Christel Poujol, Jeremie Teillon and Sebastien Marais for assistance with SP8-STED-FLIM and SP5-2P. We would also like to thank Alexandre Martinière, Yohann Boutté, and Sébastien Mongrand for reading and commenting on the article. All light and electron imaging were done at the Bordeaux Imaging Center, member of the national infrastructure France-BioImaging supported by the French National Research Agency (ANR-10-INBS-04).

Funding: This work was supported by the European Research Council (ERC) under the European Union's Horizon 2020 research and innovation program (project 772103-BRIDGING to E.M.B. and 101001097-LIPIDEV to Y.J.); the National Agency for Research (Grant ANR-18-CE13-0016 STAYING-TIGHT to E.M.B and Y.J.; ANR-21-CE13-0016-01 DIVCON to A.T. and E.M.B; ANR-18-CE13-0025-02 caLIPSO to Y.J.); the Human Frontier Science Program (project RGP0002/2020, E.M.B.); the French government in the framework of the IdEX Bordeaux University "Investments for the Future" program / GPR Bordeaux Plant Sciences (E.M.B.).

Author contributions:

Conceptualization: J.P-S., M. S., Y.J., E.M.B

Methodology: J.P-S., M. S., M.G., S.S., G.D., L.F., F.I., J.T., A.T., Y.J., E.M.B

Validation: J.P-S., M. S., A.T., Y.J., E.M.B

Investigation: J. P-S, M.S., M.G., S.S., G.D. V.D., M.P.P., Z. P.L., H.M., A.P., L. F., M.S.G., P. C-Q, T. S.M., F.I., V.W., M.D., L.B., C.C., M.Z., Y. L., M.Z.

Supervision: Y.J., E.M.B.

Funding acquisition: A.T., Y.J., E.M.B,

Writing – original draft: J.P-S, M.S., Y.J., E.M.B

Writing – review & editing: J.P-S, M.S., V.D., A.P., P. C-Q, M.P.P., J.T., Y.H., A.T., Y.J., E.M.B

Declaration of interests: The authors declare no competing interests.

Data and materials availability: All data are available in the main text or the supplementary materials

Methods

- Plant material

Arabidopsis thaliana, accession Columbia, (which we are referring to as wild type-WT) and transgenic lines (all in Columbia background) were surface sterilized, vernalized at 4C during 2 days and grown vertically on solid half-strength Murashige and Skoog media supplemented with vitamins (2.15 g/L), MES (0.5 g/L), sucrose (10 g/L) and plant agar (7 g/L), pH 5.7 for 6 days at 22°C in a 16-h light/8-h dark cycle with 70% relative humidity and a light intensity of 200 µmol x m^{-2} x s^{-1} prior to use. Recently harvested, synchronized seeds were used for all phenotypical analysis. *Nicotiana benthamiana* plants were grown in insect proof greenhouse with 18/25°C night/day.

- Cell culture

Arabidopsis (*Landsberg erecta*) culture cells were cultivated as described in Bayer et al. (Bayer et al., 2004) under constant light (20 µE/m/s) at 22°C. Cells were used for PLASMODESMATAextraction at 7 days old.

- Cloning and plasmid construction

In this study, the constructs employed were derived from Col-0 cDNA/genomic DNA, or were synthesized. The promoter sequences were integrated into pDONR-p4RP1, while the genes and fluorescent tags were integrated into either pDONR221 or pDONR-P2RP3, utilizing the MultiSite-Gateway cloning system. For the development of an inducible genome editing vector, plasmids containing the inducible RPS5A promoter, codon-optimized and RFP-tagged Cas9, along with two sgRNAs, were assembled using the Gateway system. The assembly of all constructs was carried out through multi-Gateway reactions, wherein three segments were cloned into the destination vector, pLOK180, which facilitated a red seed-coat selection marker.

The expression vectors were introduced into *Agrobacterium tumefaciens* strain GVG3101, which was then used to transform Arabidopsis Col-0 or mctp mutants (as indicated in the figure legends) through the floral dip method, as previously described (Clough and Bent, 1998). Transformed seeds were selected based on the presence of either red seed coat or BASTA resistance, depending on the selection marker used.

- Transient expression in *Nicotiana benthamiana*

The abaxial side of leaves of 3- to 4-week-old *Nicotiana benthamiana* plants were pressure-infiltrated with GV3101 agrobacterium strains carrying the different constructs. Prior to infiltration, the agrobacterium cultures were grown overnight in Luria and Bertani medium supplemented with rifampicin (50 mg/mL), gentamycin (25 mg/mL), and the construct-specific antibiotic at 28°C. Subsequently, the cultures were diluted to 1/10 in the same growing medium (without Rifampicin) and further cultivated until the optical density at 600 nm (OD600) reached approximately 0.6-0.8. The bacterial cells were then collected through centrifugation at 3000g for 5 min, followed by resuspension in agroinfiltration solution (10 mM MES, pH 5.6, 10 mM MgCl2, and 1 mM acetosyringone) and incubated for 2h at room temperature and in the dark. For infiltration of individual constructs, a final OD600 of 0.3 was used. For co-infiltration of two constructs, and OD600 of 0.2 each was used. Additionally, the ectopic silencing suppressor p19 was co-infiltrated in all the cases at an OD600 of 0.05. Post-infiltration, plants were kept in the same growing conditions as before for 2 more days; then leaf-discs were collected from the N. benthamiana leaves and subjected to imaging at room temperature.

- Lattice light sheet

The Lattice Light Sheet Microscope (LLSM) was built according to the technical information provided by the group of E. Betzig at Janelia Research Campus, Howard Hughes Medical Institute (HHMI), USA. The lattice light sheet was focused by a custom excitation objective 28.6× 0.66 numerical aperture 3.74-mm (Special Optics). Fluorescence was collected with a CFI Apo LWD 1.1 numerical aperture 25× 2.0-mm detection objective (Nikon) and imaged on a scientific complementary metal-oxide semiconductor (sCMOS) ORCA-Flash4.0 V2 camera (Hamamatsu). The annular mask minimum and maximum numerical apertures were 0.35 and 0.4, respectively, thus creating a light sheet with a uniform thickness over length > 30µm. All images were acquired in dithered square lattice mode. We characterized the LLSM optical resolution at l_{em}=510nm using 170nm diameter beads. We found 275 +/- 5 nm and 690 +/- 10 nm, laterally and axially respectively. Images were acquired at ~10 to 20 µm below the surface of the root. Fast sample translation with a piezo stage was used to acquire Z stacks with a step of 300 nm. Typical laser power incident on the excitation objective is ~ 0.4mW. The raw data are 3D deconvolved with an open-source Richardson Lucy (RL) algorithm (https://github.com/dmilkie/cudaDecon) using an experimental PSF. The RL software is bundled into LLSpy, a python LLSM data processing and visualization toolbox (https://github.com/tlambert03/LLSpy). Deconvolution runs on a CUDA compatible GPU graphics card. A 3x3 median filter (noisy pixel removal) followed by background subtraction is applied before RL deconvolution with 10 iterations.

- Laser Scanning Confocal Microscopy

In the conducted live-imaging experiments, a Zeiss LSM 880 confocal microscope equipped with 40x and 63x oil-immersion objectives, as well as 40x water immersion objectives, was employed. The microscope was controlled using ZEN Black 2011 software. The experiments were carried out at a controlled temperature ranging from 22 to 24 C.

To detect GFP in the confocal mode, a filter with an excitation (Ex) wavelength of 488 nm and an emission (Em) range of 505-550 nm was utilized. For the detection of tagRFP or propidium iodide (PI) fluorescence, a filter with an Ex wavelength of 556 nm and an Em range of 570-625 nm was employed. To detect YFP fluorescence, a filter with an excitation (Ex) wavelength of 514 nm and an emission (Em) range of 520-570 nm was utilized when imaging YFP alone. When YFP was imaged together with a red reporter, we used the settings already described for GFP.

For Airyscan imaging, GFP or YFP fluorescence was detected using an excitation (EX) wavelength of 488 nm and an emission bandpass (Em BP) range of 420-480 nm in combination with 495-550 nm. On the other hand, for the detection of PI an excitation (EX) wavelength of 488 nm and an emission (Em) range of 620-700 nm in combination with a long pass (LP) filter at 645 nm were used. For callose imaging, atto550 excitation was done with 561 nm power excitation and fluorescence collected between 566 and 700 nm. Callose deposition at PLASMODESMATAwas quantified with Fiji software and signal from the forming cell plae was excluded as indicated in Figure 3. Calcoflour aquisition was done by 405nm excitation and collected at 410-480nm.

To prevent signal cross-talk, image acquisition occurred by frame when two colors were imaged simultaneously.

- Cryofixation and freeze -substitution

Five-day old seedlings of WT, *mctp3/4* and *mctp3/4/6* were grown vertically MS ½. Roots were taken and cryofixed in 20% BSA filled copper platelets (100 nm deep and 1.5 mm wide) with EM PACT1 high-pressure freezer (Leica). Subsequently, the root tissues were harvested and subjected to cryopreservation by rapidly freezing them using a high-pressure freezer (Leica EM PACT1) equipped with copper platelets (100 nm deep and 1.5 mm wide) filled with 20% bovine serum albumin (BSA) solution. The cryofixed samples were then subjected to freeze-substitution within an AFS2 system (Leica) maintained at -90 °C. The cryosubstitution process involved immersing the samples in a cryosubstitution mixture containing 0.36% uranyl acetate in pure acetone for a duration of 24 hours. Subsequently, the temperature was gradually increased at a rate of 3 °C per hour until it reached -50 °C and held steady for 3 hours. To ensure thorough substitution, the cryosubstitution mixture was replaced with pure acetone and later pure ethanol, with each solvent being applied for three 10-minute washes. The copper platelets were intentionally retained to prevent any potential loss of the samples. Infiltration of the specimens was carried out using a series of increasing concentrations of HM20 Lowicryl resin (Electron Microscopy Science), including 25% and 50% (1 hour each), 75% (2 hours), and finally 100% (overnight, 4 hours, 48 hours, with fresh resin for each bath). Following infiltration, the samples were polymerized under ultraviolet light for 24 hours at -50 °C, after which the temperature was incrementally raised at a rate of 3 °C per hour until it reached 20 °C, where it was maintained for an additional 6 hours.

- Tomography and Transmission Electron Microscopy

Fixed root embedded in Spurr resin blocks were sectioned longitudinally into slices with a thickness of 90 nm using an EM UC7 ultramicrotome (Leica) These sections were then delicately positioned onto 200 mesh copper grids. Subsequent observations were conducted employing a FEI TECNAI Spirit 120 kV electron microscope. For plasmodesmata structure status we analyzed 15-30 bridges from WT and mctp3/4/6.

For the purposes of tomographic analysis, a protocol in accordance with the approach outlined by Nicolas et al., 2017a was employed. To facilitate image alignment during the tomography process, sections were coated with 5 nm colloidal fiducials. A series of tilt images spanning an angular range from -65° to 65° was acquired with a 1° angular increment using the FEI 3D explore tomography software. Subsequently, tomographic reconstructions were generated utilizing the eTomo software (http://bio3d.colorado.edu/imod/). Segmentation tasks were carried out employing the 3dMOD software (https://bio3d.colorado.edu/imod/doc/3dmodguide.html).

- Forester Resonance Energy Transfer-Fluorescence Lifetime Imaging (FRET-FLIM)

The confocal microscope used for FRET FLIM was a Leica SP8 WLL2 on an inverted stand DMI6000 (Leica Microsystems, Mannheim, Germany), using objectives HC Plan Apo CS2 40X oil NA 1.30. The confocal microscope was equipped of a pulsed white light laser 2 (WLL2) with freely tuneable excitation from 470 to 670 nm (1 nm steps) and a pulsed diode at 440 nm and also a diode laser at 405 nm.

The scanning was done using either a conventional scanner (10Hz to 1800 Hz) or a resonant scanner (8000Hz). The microscope was composed of 2 internal photomultiplier tubes (PMT), 2 internal hybrid detectors and 1 external PMT for transmission. For excitation of the donor pMCTP4::e-YFP- MCTP4, 516nm laser was used. The confocal microscope was equipped with the FALCON module for FLIM measurements. We used 5 iterations in order to acquire enough photon counts (10-4). Monoexponential fit was applied for both donor alone and donor with the acceptor (pMCTP3::mCherryMCTP3) and values were extracted only from the plasmodesmata signal.

- Two-photon microscopy and cell diffusion assay with DRONPA-s

5-day-old 35S::DRONPA-s seedlings was cultivated on ½ MS plates under long-day conditions at 21 °C with 70% humidity. Subsequently, these seedlings were transferred to either DMSO or 200nM Brassinolide plates for an additional 24 hours. The root tips of the seedlings were subjected to analysis using a Leica TCS SP5-Multi photon confocal microscope setup. Prior to imaging, the plants underwent a 2-minute incubation in a 1/500 propidium iodide (PI) solution in water. PI was excited at 488 nm and its emissions were detected at 620-700 nm. Leica LAS AF software was employed for the quantification of fluorescence intensities.

The movement of DRONPA-s was captured as follows:

1. DRONPA-s deactivation: Root tips were illuminated with 488 nm light for 45 seconds at 70% of the total laser intensity using an argon laser (20mW, Leica Microsystems).
2. DRONPA-s activation: Three Regions of Interest (ROIs), each corresponding to a single cell per root, were selected at the cell center to avoid activating adjacent cells. These ROIs were exposed to 5 seconds of 800 nm light using a two-photon IR (Titane-Saphir pulsating laser). The laser power used was approximately 2.6W with a 20% gain.
3. DRONPA-s acquisition: Detection was conducted 2 seconds after the single cell activation and continued for 120 seconds, using a 20% 488 nm argon laser at an emission range of 500-575 nm.

DRONPA-s movement analysis involved measuring mean fluorescence intensities from the activated cell and the two adjacent cells using ImageJ. DRONPA movement was calculated based on the fluorescent signal transferred from the activated cell to the adjacent cells. Any X-Y drifts were corrected with the StackReg plugin. Following normalization and background subtraction, the values were converted into a percentage of the average fluorescence from the two adjacent cells. The activated cell was considered to have 100% DRONPA-s molecules activated in the ROI. A total of more than 20 roots were analyzed, with 2-3 ROIs per root."

- Fluorescence Recovery After Photobleeching

PI permeability assessments were made using FRAP on six day-old Arabidopsis root tips co-stained with CFDA (50µg/mL) and Propidium iodide.Roots were incubated in an aqueous CFDA solution for 5 minutes, then successively washed out in 3 water baths and mounted with propidium iodide in water for imaging FRAP experiments were conducted using a Zeiss LSM 880 confocal microscope, which was equipped with a Zeiss CPL APO x 40 oil-immersion objective (numerical aperture 1.3). To excite CFDA, a 488 nm wavelength was utilized with 100% of argon laser power, and the fluorescence emission was collected within the 505–550 nm range using a GaAsp detector. Photobleaching was performed on rectangular regions of interest (ROIs) encompassing three epidermal cells, with the exciting laser wavelengths set to 100%. The FRAP procedure involved capturing 10 pre-bleach images, followed by 15 iterations of bleaching, with a pixel dwell time of 1.31 µs. Subsequently, 90 post-bleach images were acquired. The recovery profiles were subjected to background subtraction and then double normalization through the FRAP analysis website : https://easyfrap.vmnet.upatras.gr/?AspxAutoDetectCookieSupport=1.

- co-Immunoprecipitation in *Nicotiana benthamiana*.

The appropriate constructs were transiently expressed in Nicotiana bentamiana (see Transient expression in *Nicotiana benthamiana* section). Two plants per construct combination and two whole leaves per plant were agroinfiltrated. Using a puncher, 10 leaf-discs were collected for each leaf, so 40 leaf-discs per construct combination, and immediately frozen in liquid nitrogen (aprox 0.5 g of tissue). Frozen tissue was grinded using mortar and pestle and total proteins were extracted with 1 mL of extraction buffer (150 mM Tris-HCl, pH 7.5; 150 mM NaCl; 10 % glycerol; 10 mM EDTA, pH 8; 1mM NaF; 1 mM Na2MoO4; 10 mM DTT; 0.5 mM PMSF; 1% (v/v) P9599 protease inhibitor cocktail (Sigma); 1 % (v/v) Igepal) by incubating during 40 min at 4 C with continuous mixing in an end-over-end rocker. Samples were centrifuged for 20 min at 4C and 9,000 g. Supernatants were filtered by gravity through Poly-PrepChromatography Columns (#731-1550 Bio-Rad). For each sample, 50 uL of the filtered supernatant were collected and mixed with 50 uL of Laemmli buffer (Tris-HCl pH 6.8 125 mM; 4% SDS; 20 % (v/v) glycerol; 2 % (v/v) beta-mercaptoethanol; 0.01 % bromophenol blue) for immunoblot analysis as input. The remaining filtered supernatants were mixed in a 1:1 proportion with wash buffer (extraction buffer without Igepal) to reach a final concentration of 0.5 % Igepal in the samples before adding the GFP-Trap agarose beads (as recommended by the manufacturer to avoid nonspecific binding). 15 uL of equilibrated GFP-Trap agarose beads were added to each sample and incubated during 2 h at 4 C with continuous mixing. After incubation, samples were centrifuged 30 s at 500 g to precipitate the beads Then beads were washed 3 times with wash buffer. After the third wash, a final centrifugation during 30 s at 2000 g was performed and the suppernantant was discarded. Finally, immunoprecipitated proteins were eluted by incubating the beads with 50 uL of Laemmli buffer at 70 C for 20 min followed by 2 min centrifugation at 2500 g and recovery of the supernatant. Input and immunoprecipitated samples were analyzed by western blot.

- Lipid inhibitor treatments

PAO treatment was used to inhibit PI4kinases (Simon et al., 2016b). 25-30 minutes of 60µM PAO was used to 5 days old 35S::DRONPA-s in WT and *mctp4/3* mutants background then imaged. Wortmanin was used to inhibit PI3 kinase (Gomez et al., 2022) at a concentration of 10µM for 40 minutes and YM 201653 was used to inhibit PI3,5kinase at a concentration of 2µM and treated for 1 hour.

- Environmental and hormonal triggers with Brasinosteroids and NaCL

For Brasinolide (BL) and Brassinazole (BRZ) treatment 4 days old roots of 35S::DRONPA-s in WT and mctp4/3 background were transferred in ½ MS plate containing 200nM BL or 1µM BRZ and grown for 24h before imaging. DMSO was used as a mock solution/ Salt treatment was performed by growing the same lines for 5 days and 20mM NaCl was applied 15 minutes before imaging. Water was used as a control solution.

- Callose immunostaining

Arabidopsis seedlings were vertically cultivated on ½MS agar plates for a duration of 4 days. Subsequently, they were transferred to fresh media and subjected to various treatments for an additional 24 hours. The treatments included 200 nM BR, 1 µM BRZ, DMSO mock, and a 15-minute exposure to 20mM NaCl.

The immunolocalization procedure was performed following a previously published protocol (Pendle and Benitez-Alfonso, 2015). All solutions were prepared in microtubule stabilization buffer (MTSB), comprising 50 mM PIPES, 5 mM EGTA, 5 mM MgSO4, and adjusted to pH 7 with KOH. Seedlings were fixed in 4% (v/v) paraformaldehyde in for 1h followed by 4 washes with MTSB. Root tips were then excised and mounted on microscopy slides coated with poly-lysine.

Immunolabelling was performed using the Immunorobot InSituPro VSI from Protigene. Briefly, the procedure includes cell-wall permeabilization with driselase 2% during 15 min and plasma membrane permeabilization by 10 % DMSO and 3 % Igepal during 1 h. To prevent nonspecific binding, the samples were subjected to a blocking step using 5% neutral donkey serum before incubation with the primary antibody. The callose antibody (obtained from Australia Biosupplies) was appropriately diluted to 1/500 in MTSB supplemented with 5% (v/v) neutral donkey serum and incubated with the samples at room temperature for 4 hours.

For the subsequent step, the secondary anti-mouse antibody, coupled to atto550 (Merk) or alexa fluor 594, was diluted to 1/1000 in MTSB buffer containing 5% (v/v) neutral donkey serum. This antibody solution was then applied to the samples and allowed to incubate for 1 hour.

- Root growth assay

Phenotyping of the root growth rate (Schindelin et al., 2012; Slovak et al., 2014; Platre et al., 2023)**.** Wild type, single (*mctp3-2, mctp3-1, mctp4-1, mctp4-2, mctp6-1*), double (*mctp3-2/mctp4-1, mctp3-1/mctp4-1, mctp3-2/mctp6-1*) and triple (*mctp3-2/mctp4-1/mctp6-1*) mutant seeds were sowed in 12-cm x 12-cm square plates filled with 1/2 MS medium containing 0.8% of agar and 0.5% of sucrose and were stratified for 2-3 days at 4°C before being transfer to a growth chamber. Six days after planting, about 20 seedlings were transferred using forceps to an imaging chamber (Lab-Tek, Chambers #1.0 Borosilicate Coverglass System, catalog number: 155361) filled with the identical medium described above. Note that the transfer took about 45-60 seconds. Images were acquired every minute for 6 hours, in brightfield conditions using a Keyence® microscope model BZ-X810 with a BZ NIKON Objective Lens 2X CFI Plan-Apo Lambda (Platre et al., 2021).

The same plants were then transferred to 12-cm x 12-cm square plates filled with 1/2 MS medium containing 0.8% of agar and 0.5% of sucrose and grown to three more days and scanned to calculate the root growth rate per day.

*Quantification of the root growth rate***.** For time lapse analysis of the root growth rate the script was used " SCRIPT_MCTP" and is available on https://github.com/mplatre/SCRIPT_MCTP.git. To calculate the root growth rate per day the plates were scanned using BRAT software (Slovak et al., 2014). We then calculated the root length for three days and divided by three to evaluate the root growth rate per day using Fiji (Schindelin et al., 2012).

- Liposome binding assays

Experiment was performed as in Pérez-Sancho et al. (Pérez-sancho et al., 2016), with small modifications:

Protein production and purification

The C2B domain of MCTP4 was expressed as His-tagged protein using the expression vector pET28 and transformed in E.Coli BL21 (DE3). A 5 mL culture of transformed bacteria in LB medium with 50 µg/mL of Kanamycin (Kan) was grown overnight at 37 °C with continuous rotation at 200 rpm. 50 mL LB medium + Kan was inoculated with 2 mL of the overnight grown culture and incubated at 37 °C for 2-3 h, ultil the OD600 was between 0.6 and 0.8. Then, the expression of MCTP4-C2B was induced by adding 100µM IPTG to the culture and incubating overnight at 18 °C. A sample of the culture before and after protein induction was collected to assay protein production by SDS-PAGE. Cell culture was centrifuged at 1600 g during 15 min and the pellet (1 g) was resuspended in 3 mL of buffer A (HEPES NaOH 50 mM pH 7.6, NaCl 150 mM, Glycerol 10%, DTT 1 mM). Cells were disrupted by sonication (three cycles of 2 min, with 20 s on and 40 s off and 60 % amplitude, keeping the tube on ice) and the suspension was centrifuged at 100 000 g and 4 °C for 30 min. The supernatant was collected, mixed with 600 µL of Ni-NTA beads slurry (300 µL beads) and 125 µL of Benzoase (250 U/ µL), and incubated for 1 h at 4°C wit rotation to allow proteins to bind to the beads. The mixture was centrifuged at 5000 g and 4 °C for 5 min and the pelleted beads were washed 5 times with 1.5 mL of buffer A. Finally, proteins were eluted with buffer A containing 500 mM imidazole and their concentration was determined by Nanodrop (Mw 21278 and Ɛ 32430).

Liposome preparation

Liposomes of different composition were prepared by mixing the corresponding lipids stocks in chloroform. Lipid stocks were: PC at 10 mg/mL, PS at 10 mg/mL, PI(4)P at 5 mg/mL, PA at 10 mg/mL, PI(4,5)P2 at 5 mg/mL, and DOPE-Rho (1,2-dioleoyl-sn-glycero-3-phosphoethanolamine conjugated to rhodamine) at 1 mg/mL (used to visualize the lipid fraction during the preparation); and were mixed as indicated in the table below:

	PC (µL)	PS (µL)	PI(4)P (µL)	PA (µL)	PI(4,5)P2 (µL)	DOPE-Rho (µL)
PC	78	0	0	0	0	13
PC:PS	62	20	0	0	0	13
PC:PS:PI(4)P	42	20	40	0	0	13
PC:PS:PA	50	20	0	7	0	13
PC:PS:PI(4,5)P2	42	20	0	0	44	13

Lipid mixtures were dried as a thin layer using a nitrogen stream and the lipid layers were resuspended in 1 mL of buffer A by vortexing at room temperature during 20 min. Then, they were subjected to 5 cycles of freezing in liquid nitrogen and thawing in a water bath at 37 °C and extruded 10 times through an 800 nm pore size polycarbonate membrane.

Liposome binding and sedimentation

10 µg of purified MCTP4-C2B and 40 µL of liposomes were mixed in buffer A containing 10 mM CaCl2 (1 mix for each different liposome composition) until a final volume of 200 µL and incubated at room temperature for 15 min without agitation. Large multilamellar vesicles (and the proteins bound to them) were collected by centrifugation at 300 000 g and 4°C for 45 min. 195 µL of supernatants were recovered and the pellets were resuspended in 195 µL of buffer A. Supernatant and resuspended-pellet fractions were mix with Commassie blue buffer and run into SDS-PAGE for protein separation and quantification. Only one band corresponding to the C2B domain of MCTP4 was observed for each of the samples and each of the repetitions of the experiment. Gels were imaged using a Bio-rad's stain-free imager on TGX-Stain-Free acrylamide gels and proteins quantified using Fiji.

- Plasmodesmata purification and lipid analysis via liquid chromatography-tandem mass spectrometry (LC-MS/MS)

The cell wall fractions were prepared from 6-day-old Arabidopsis suspension cultured cells, following the methodology outlined by Bayer et al. (Bayer et al., 2004). However, in this study, the cell disruption process was repeated five consecutive times using the N2 cell disruption vessel, in contrast to the standard three repetitions. To obtain the plasmodesmata-enriched membrane fraction, purified wall fragments were utilized, employing the method described by (Fouillen et al., 2022). Briefly, purified cell walls were subjected to digestion with 0.7% (w/v) cellulase R10 (Karlan) in a digestion buffer comprising 10 mM MES (pH 5.5) and 4.4% mannitol, supplemented with 1 µM phenylmethylsulfonyl fluoride and a complete protease inhibitor cocktail (Roche Diagnostic). The digestion process was carried out at 37°C for 1.5 hours with continuous shaking at 50 to 100 rpm. Following the digestion step, centrifugation was performed at 5850g for 5 minutes at 4°C to separate the supernatant and pellet fractions. The pellet underwent additional washing in an excess volume of digestion buffer before undergoing a second centrifugation step. The two supernatants were combined and subjected to further centrifugation at 110,000g for 40 minutes at 4°C. The resulting pellet, which contained plasmodesmata-derived membranes, was washed with an excess volume of cold Tris-buffered saline (TBS; 20 mM Tris-HCl, 0.14 M NaCl, and 2.5 mM KCl, pH 7.4). Finally, the pellet was resuspended in cold 1× TBS containing protease inhibitors (Roche Diagnostic). It is noteworthy that approximately 600 mL of cultured cells was employed to yield 100 µg of plasmodesmata-enriched membrane fraction. The protein amount in the samples was determined using a bicinchoninic acid protein assay with BSA as the standard. For the purification of plasmodesmata-enriched membrane fractions from cells subjected to sterol inhibitor treatment, fen was added to 5-day-old liquid cultured Arabidopsis cells at a final concentration of 250 µg/mL (stock solution 500 µg/µL in DMSO) and incubated as previously described for 48 hours before the purification process.

For anionic lipid analysis we followed the protocol described in (Genva et al., 2023). In brief, plasmodesmata fraction was incubated with 725 µL of a MeOH/$CHCl_3$/1M HCl (2/1/0.1 v/v/v) solution and 150 µL water in presence of 10 ng of 17:0-20:4 PI4P standard (Avanti). 750 µl of chloroform and 170 µl HCl 2M were then added. The samples were vigorously shaken and centrifuged. The lower phase was washed with 700 µl of the upper phase of a mix of methanol:chloroform:HCl 0.01M 1:2:0.75, vortexed and centrifuged. Then, samples were kept overnight at -20 °C.

The organic phase was transferred to a new Eppendorf and the methylation reaction was carried out. For this purpose, 50 µL of TMS-diazomethane (2M in hexane) were added to each sample. After 10 min, the reaction was stopped by adding 6 µL of glacial acetic acid. 700 µL of the upper phase of a mix of MeOH/$CHCl_3$/H_2O (1/2/0.75 v/v/v) was added to each sample which was then vortexed and centrifuged (1500 x *g*, 3 min). The upper phase was removed and the washing step was repeated once. Finally, the lower organic phases were transferred to new Eppendorf. Following the addition of 100 µL MeOH/H2O (9:1 v/v), the samples were concentrated under a gentle flow of air until only a drop remained. 80 µL of methanol were added to the samples, which were submitted to ultrasounds for 1 minute, before adding 20 µL water, and be submitted to 1 more-minute ultrasound. The samples were finally transferred to HPLC vials for analysis.

Analysis of methylated anionic phospholipids (Genva et al. 2023) were performed using a liquid chromatography system (1290 Infinity II, Agilent) coupled to a QTRAP 6500 mass spectrometer (ABSciex). The chromatographic separation of anionic phospholipid species was performed on a reverse phase C18 column (SUPELCOSIL ABZ PLUS; 10 cm x 2.1 mm, 3µm, Merck) using methanol/water (3/2) as solvent A and isopropanol/methanol (4/1) as solvent B at a flow rate of 0.2 mL/min. All solvents are supplemented with 0.1% HCCOOH and 10 mM ammonium formate. 10 µL of samples were injected and the percentage of solvent B during the gradient elution was the following: 0–20 min, 45%; 40 min, 60%; 50 min, 80%. The column temperature was kept at 40 °C. Mass spectrometry analysis was performed in the positive ionization mode. Mass spectrometry data were treated using the MultiQuant software (ABSciex). Nitrogen was used for the curtain gas (set to 35), gas 1 (set to 40), and gas 2 (set to 40). Needle voltage was at +5500 V with needle heating at 350 °C; the declustering potential was +10 V. The collision gas was also nitrogen; was set between 26 to 45 eV according to the lipid classes.

- Molecular dynamics

Membrane Creation

We used the Insane program (Jumper et al., 2021) to generate three membranes with a composition representative of the plasma membrane: (70%,68%,64%) phosphatidylcholine (PC), 20% Sitosterol, 10% phosphatidylserine (PS), (0%, 2%, 6%) P(I)4P. Two lipids present in our modeled membrane were not present in the Martini 3 topology library: PS of plants that have a longer tail (18:2 24:1) and sitosterol. The topology for PS (18:2 24:1) was created by analogy, using the topology files of PIPS and DNPS. The Sitosterol model was obtained from Paulo C. T. Souza and Luís Borges Araújo following the recent parameterization of cholesterol in MARTINI 3 (Borges-Araújo et al., 2023).

Protein Setup

Three prediction tools, AlphaFold Monomer (Jumper et al., 2021), AlphaFold Multimer (Souza et al., 2021), and RosettaFold (Baek et al., 2021), were employed to determine the 3D structure of MCTP4. These methods converged on a single solution for the C2 domains.

All simulations were conducted using Gromacs 2023.2 (https://manual.gromacs.org/2023.2/release-notes/index.html), supplemented with the Colvar plugin. The Martini 3 force field (Souza et al., 2021) was utilized. We applied a constraint network to the protein to stabilize the 3D structure of the cytoplasmic domain. The protein's center of mass was positioned 10 nm from the membrane. We replicated each condition five times. Each system underwent minimization and equilibration at 300K. The protocol included an initial phase of energy minimization, followed by multi-stage equilibration, and concluded with a production simulation. Energy minimization was performed in two iterations of 5,000 steps each, using the steepest descent method. The simulations were then equilibrated in five stages, using time steps of 2, 5, 10, 15, and 20 fs. A target temperature of 300 K was maintained using the v-rescale thermostat, with a coupling constant of 1 ps. A semi-isotropic pressure of 1 bar was maintained using the Parrinello-Rahman barostat, with a compressibility of 4.5 × 10^-5 bar^-1 and a relaxation time constant of 12 ps. Long-range interactions were handled with a cutoff radius of 1.1 nm for both van der Waals and Coulombic interactions, implementing a switching function from 1.0 nm for van der Waals. The production simulations were executed in an NPT ensemble with a time step of 20 fs for a total simulation time of 3 microseconds.

• Quantification and Statistical Analysis

Statistical analyses were performed in GraphPad Prism (GraphPad Software). All experiments were independently repeated a minimum of 2–3 times (indicated in figure legends). Data are expressed as median unless specified in the figure legends.

References

Abou-Saleh RH, Hernandez-Gomez MC, Amsbury S, Paniagua C, Bourdon M, Miyashima S, Helariutta Y, Fuller M, Budtova T, Connell SD, et al (2018) Interactions between callose and cellulose revealed through the analysis of biopolymer mixtures. Nat Commun 9: 4538

Amsbury S, Kirk P, Benitez-Alfonso Y (2017) Emerging models on the regulation of intercellular transport by plasmodesmata-associated callose. J Exp Bot 69: 105–115

Baek M, DiMaio F, Anishchenko I, Dauparas J, Ovchinnikov S, Lee GR, Wang J, Cong Q, Kinch LN, Dustin Schaeffer R, et al (2021) Accurate prediction of protein structures and interactions using a three-track neural network. Science 373: 871–876

Balla T (2018) Ca2+ and lipid signals hold hands at endoplasmic reticulum–plasma membrane contact sites. J Physiol 596: 2709–2716

Bayer E, Thomas CLL, Maule AJJ (2004) Plasmodesmata in Arabidopsis thaliana suspension cells. Protoplasma 223: 93–102

Benavente JL, Siliqi D, Infantes L, Lagartera L, Mills A, Gago F, Ruiz-López N, Botella MA, Sánchez-Barrena MJ, Albert A (2021) The structure and flexibility analysis of the Arabidopsis synaptotagmin 1 reveal the basis of its regulation at membrane contact sites. Life Sci Alliance. doi: 10.26508/LSA.202101152

Benitez-Alfonso Y, Faulkner C, Pendle A, Miyashima S, Helariutta Y, Maule A (2013) Symplastic intercellular connectivity regulates Llteral root patterning. Dev Cell 26: 136–147

Bharathan NK, Giang W, Hoffman CL, Aaron JS, Khuon S, Chew TL, Preibisch S, Trautman ET, Heinrich L, Bogovic J, et al (2023) Architecture and dynamics of a desmosome–endoplasmic reticulum complex. Nat Cell Biol 25: 823–835

Bian X, Saheki Y, De Camilli P (2018) Ca 2+ releases E-Syt1 autoinhibition to couple ER -plasma membrane tethering with lipid transport . EMBO J 37: 219–234

Borges-Araújo L, Borges-Araújo AC, Ozturk TN, Ramirez-Echemendia DP, Fábián B, Carpenter TS, Thallmair S, Barnoud J, Ingólfsson HI, Hummer G, et al (2023) Martini 3 Coarse-Grained Force Field for Cholesterol. J Chem Theory Comput. doi: 10.1021/acs.jctc.3c00547

Brault ML, Petit JD, Immel F, Nicolas WJ, Glavier M, Brocard L, Gaston A, Fouché M, Hawkins TJ, Crowet J-M, et al (2019) Multiple C2 domains and transmembrane region proteins (MCTPs) tether membranes at plasmodesmata. EMBO Rep e47182

Cheval C, Faulkner C (2018) Plasmodesmal regulation during plant–pathogen interactions. New Phytol 217: 62–67

Chung J yun, Torta F, Masai K, Lucast L, Czapla H, Tanner LB, Narayanaswamy P, Wenk MR, Nakatsu F, De Camilli P, et al (2015) PI4P/phosphatidylserine countertransport at ORP5- and ORP8-mediated ER – plasma membrane contacts. Science 349: 428–432

Clough SJ, Bent AF (1998) Floral dip : a simplified method for Agrobacterium-mediated transformation of Arabidopsis thaliana. Plant J 16: 735–743

Collado J, Kalemanov M, Martinez-Sanchez A, Campelo F, Baumeister W, Stefan CJ, Fernandez-Busnadiego R (2019) Tricalbin-Mediated Contact Sites Control ER Curvature to Maintain Plasma Membrane Integrity. SSRN Electron J 1–61

Cui W, Lee J-YY (2016) Arabidopsis callose synthases CalS1/8 regulate plasmodesmal permeability during stress. Nat Plants 2: 16034

Daum G, Medzihradszky A, Suzaki T, Lohmann JU (2014) A mechanistic framework for non-cell autonomous stem cell induction in Arabidopsis. Proc Natl Acad Sci U S A 111: 14619–24

Deinum EE, Mulder BM, Benitez-Alfonso Y (2019) From plasmodesma geometry to effective symplasmic permeability through biophysical modelling. Elife 8: 1–40

Ding B, Turgeon R, Parthasarathy M V. (1992) Substructure of freeze-substituted plasmodesmata. Protoplasma 169: 28–41

Dong R, Saheki Y, Swarup S, Lucast L, Harper JW, De Camilli P (2016) Endosome-ER contacts control actin nucleation and retromer function through VAP-dependent regulation of PI4P. Cell 166: 408–423

Eden ER, Sanchez-Heras E, Tsapara A, Sobota A, Levine TP, Futter CE (2016) Annexin A1 tethers membrane contact sites that mediate ER to endosome cholesterol transport. Dev Cell 37: 473–483

Eden ER, White IJ, Tsapara A, Futter CE (2010) Membrane contacts between endosomes and ER provide sites for PTP1B-epidermal growth factor receptor interaction. Nat Cell Biol 12: 267–72

Faulkner C, Petutschnig E, Benitez-Alfonso Y, Beck M, Robatzek S, Lipka V, Maule AJ (2013) LYM2-dependent chitin perception limits molecular flux via plasmodesmata. Proc Natl Acad Sci U S A 110: 9166–70

Fernandez-Calvino L, Faulkner C, Walshaw J, Saalbach G, Bayer E, Benitez-Alfonso Y, Maule A (2011) Arabidopsis plasmodesmal proteome. PLoS One 6: e18880

von Filseck JM, Vanni S, Mesmin B, Antonny B, Drin G (2015) A phosphatidylinositol-4-phosphate powered exchange mechanism to create a lipid gradient between membranes. Nat Commun 6: 1–12

Fouillen L, Claverol S, Bayer E, Grison SM (2022) Isolation of plasmodesmata membranes for lipidomic and proteomic analysis. Method Mol Biol 2457: 189–207

Friedman JR, Lackner LL, West M, DiBenedetto JR, Nunnari J, Voeltz GK (2011) ER tubules mark sites of mitochondrial division. Science 334: 358–362

Gao C, Liu X, Storme N De, Martens HJ, Schulz A, Liesche J, Gao C, Liu X, Storme N De, Jensen KH, et al (2020) Directionality of Plasmodesmata-Mediated Transport in Arabidopsis Leaves Supports Auxin Report Directionality of Plasmodesmata-Mediated Transport in Arabidopsis Leaves Supports Auxin Channeling. Curr Biol 30: 1970-1977.e4

Gaudioso-Pedraza R, Beck M, Frances L, Kirk P, Ripodas C, Niebel A, Oldroyd GEDD, Benitez-alfonso Y, de Carvalho-Niebel F, Carvalho-niebel F De, et al (2018) Callose-regulated symplastic communication coordinates symbiotic root nodule development. Curr Biol 28: 3562-3577.e6

Genva M, Fougère L, Bahammou D, Mongrand S, Boutté Y, Fouillen L (2023) A global LC–MS2-based methodology to identify and quantify anionic phospholipids in plant samples. Plant J. doi: 10.1111/tpj.16525

Gerlitz N, Gerum R, Sauer N, Stadler R (2018) Photoinducible DRONPA-s : a new tool for investigating cell – cell connectivity. Plant Physiol 94: 751–766

Giordano F, Saheki Y, Idevall-Hagren O, Colombo SF, Pirruccello M, Milosevic I, Gracheva EO, Bagriantsev SN, Borgese N, De Camilli P (2013) PI(4,5)P2-dependent and Ca2+-regulated ER-PM interactions mediated by the extended synaptotagmins. Cell 153: 1494

Gisel A, Barella S, Hempel FD, Zambryski PC (1999) Temporal and spatial regulation of symplastic trafficking during development in Arabidopsis thaliana apices. Development 126: 1879–1889

Gombos S, Miras M, Howe V, Xi L, Pottier M, Kazemein Jasemi NS, Schladt M, Ejike JO, Neumann U, Hänsch S, et al (2023) A high-confidence Physcomitrium patens plasmodesmata proteome by iterative scoring and validation reveals diversification of cell wall proteins during evolution. New Phytol 238: 637–653

Gomez RE, Chambaud C, Lupette J, Castets J, Pascal S, Brocard L, Noack L, Jaillais Y, Joubès J, Bernard A (2022) Phosphatidylinositol-4-phosphate controls autophagosome formation in Arabidopsis thaliana. Nat Commun. doi: 10.1038/s41467-022-32109-2

Grison MS, Kirk P, Brault ML, Wu XN, Schulze WX, Benitez-Alfonso Y, Immel F, Bayer EM (2019) Plasma membrane-associated receptor-like kinases relocalize to plasmodesmata in response to osmotic stress. Plant Physiol. doi: 10.1104/pp.19.00473

Guillén-Samander A, De Camilli P (2023) Endoplasmic reticulum membrane contact sites, lipid transport, and neurodegeneration. Cold Spring Harb Perspect Biol. doi: 10.1101/cshperspect.a041257

Guseman JM, Lee JS, Bogenschutz NL, Peterson KM, Virata RE, Xie B, Kanaoka MM, Hong Z, Torii KU (2010) Dysregulation of cell-to-cell connectivity and stomatal patterning by loss-of-function mutation in Arabidopsis CHORUS (GLUCAN SYNTHASE-LIKE 8). Development 137: 1731–1741

Hamasaki M, Furuta N, Matsuda A, Nezu A, Yamamoto A, Fujita N, Oomori H, Noda T, Haraguchi T, Hiraoka Y, et al (2013) Autophagosomes form at ER-mitochondria contact sites. Nature 495: 389–393

Han X, Hyun T, Zhang M, Kumar R, Koh EJ, Kang BH, Lucas W, Kim JY (2014) Auxin-callose-mediated plasmodesmal gating is essential for tropic auxin gradient formation and signaling. Dev Cell 28: 132–146

Hernández-Alvarez MI, Sebastián D, Vives S, Ivanova S, Bartoccioni P, Kakimoto P, Plana N, Veiga SR, Hernández V, Vasconcelos N, et al (2019) Deficient endoplasmic reticulum-mitochondrial phosphatidylserine transfer causes liver disease. Cell 177: 881-895.e17

Hirabayashi Y, Kwon SK, Paek H, Pernice WM, Paul MA, Lee J, Erfani P, Raczkowski A, Petrey DS, Pon

LA, et al (2017) ER-mitochondria tethering by PDZD8 regulates Ca2+ dynamics in mammalian neurons. Science 358: 623–630

Hoffmann PC, Bharat TAM, Wozny MR, Boulanger J, Miller EA, Kukulski W (2019) Tricalbins Contribute to Cellular Lipid Flux and Form Curved ER-PM Contacts that Are Bridged by Rod-Shaped Structures. Dev Cell 51: 488-502.e8

Hunter K, Kimura S, Rokka A, Tran HC, Toyota M, Kukkonen JP, Wrzaczek M (2019) CRK2 enhances salt tolerance by regulating callose deposition in connection with PLDα1. Plant Physiol. doi: 10.1104/pp.19.00560

Johnson B, Iuliano M, Lam T, Biederer T, De Camilli P (2023) A complex of the lipid transport ER proteins TMEM24 and C2CD2 with band 4.1 at cell-cell contacts. An ER-plasma membrane complex at cell contacts. bioRxiv. doi: 10.1101/2023.12.06.570396

Johnston MG, Breakspear A, Samwald S, Zhang D, Papp D, Faulkner C, De Keijzer J (2023) Comparative phyloproteomics identifies conserved plasmodesmal proteins. J Exp Bot 74: 1821–1835

Jumper J, Evans R, Pritzel A, Green T, Figurnov M, Ronneberger O, Tunyasuvunakool K, Bates R, Žídek A, Potapenko A, et al (2021) Highly accurate protein structure prediction with AlphaFold. Nature 596: 583

Kirk P, Amsbury S, German L, Gaudioso-Pedraza R, Benitez-Alfonso Y (2022) A comparative meta-proteomic pipeline for the identification of plasmodesmata proteins and regulatory conditions in diverse plant species. BMC Biol 20: 1–21

Kitagawa M, Wu P, Balkunde R, Cunniff P, Jackson D (2022) An RNA exosome subunit mediates cell-to-cell trafficking of a homeobox mRNA via plasmodesmata. Science 375: 177–182

Kraner ME, Müller C, Sonnewald U (2017) Comparative proteomic profiling of the choline transporter-like1 (CHER1) mutant provides insights into plasmodesmata composition of fully developed Arabidopsis thaliana leaves. Plant J 92: 696–709

Kumagai K, Hanada K (2019) Structure, functions and regulation of CERT, a lipid-transfer protein for the delivery of ceramide at the ER–Golgi membrane contact sites. FEBS Lett 593: 2366–2377

Lee E, Vanneste S, Pérez-Sancho J, Benitez-Fuente F, Strelau M, Macho AP, Botella MA, Friml J, Rosado A (2019) Ionic stress enhances ER–PM connectivity via phosphoinositide-associated SYT1 contact site expansion in Arabidopsis. Proc Natl Acad Sci U S A 116: 1420–1429

Lee EK, Santana BVN, Samuels E, Benitez-Fuente F, Corsi E, Botella MA, Perez-Sancho J, Vanneste S, Friml J, Macho A, et al (2020) Rare earth elements induce cytoskeleton-dependent and PI4P-associated rearrangement of SYT1/SYT5 endoplasmic reticulum-plasma membrane contact site complexes in Arabidopsis. J Exp Bot 71: 3986–3998

Lees JA, Messa M, Sun EW, Wheeler H, Torta F, Wenk MR, De Camilli P, Reinisch KM (2017) Lipid transport by TMEM24 at ER-plasma membrane contacts regulates pulsatile insulin secretion. Science (80-). doi: 10.1126/science.aah6171

Leijon F, Melzer M, Zhou Q, Srivastava V, Bulone V (2018) Proteomic analysis of plasmodesmata from populus cell suspension cultures in relation with callose biosynthesis. Front Plant Sci. doi: 10.3389/fpls.2018.01681

Lexy RO, Kasai K, Clark N, Fujiwara T, Sozzani R, Gallagher KL (2018) Exposure to heavy metal stress triggers changes in plasmodesmatal permeability via deposition and breakdown of callose. 69: 3715–3728

Li ZP, Moreau H, Petit JD, Souza-Moraes T, Smokvarska M, Perez-Sancho J, Petrel M, Decoeur F, Brocard L, Chambaud C, et al (2023) Plant plasmodesmata bridges form through ER-driven incomplete cytokinesis. bioRxiv

Li ZP, Paterlini A, Glavier M, Bayer EM (2021) Intercellular trafficking via plasmodesmata: molecular layers of complexity. Cell Mol Life Sci 78: 799–816

Mehra P, Pandey BK, Melebari D, Banda J, Leftley N, Couvreur V, Rowe J, Anfang M, De Gernier H, Morris E, et al (2022) Hydraulic flux–responsive hormone redistribution determines root branching. Science 378: 762–768

Mellor NL, Voß U, Janes G, Bennett MJ, Wells DM, Band LR (2020) Auxin fluxes through plasmodesmata modify root-tip auxin distribution. Development. doi: 10.1242/dev.181669

Mesmin B, Bigay J, Von Filseck JM, Lacas-Gervais S, Drin G, Antonny B (2013) A four-step cycle driven by PI(4)P hydrolysis directs sterol/PI(4)P exchange by the ER-Golgi Tether OSBP. Cell 155: 830–843

Miras M, Pottier M, Schladt TM, Ejike JO, Redzich L, Frommer WB, Kim JY (2022a) Plasmodesmata and their role in assimilate translocation. J Plant Physiol 270: 153633

Miras M, Pottier M, Schladt TM, Ejike JO, Redzich L, Frommer WB, Kim JY (2022b) Plasmodesmata and their role in assimilate translocation. J Plant Physiol 270: 153633

Miyashima S, Roszak P, Sevilem I, Toyokura K, Blob B, Heo J, Mellor N, Help-rinta-rahko H, Otero S, Smet W, et al (2019) Mobile PEAR transcription factors integrate positional cues to prime cambial growth. Nature 565: 490–494

Nakajima K, Sena G, Nawy T, Benfey PN (2001) Intercellular movement of the putative transcription factor SHR in root patterning. Nature 413: 307–311

Naón D, Hernández-Alvarez MI, Shinjo S, Wieczor M, Ivanova S, de Brito OM, Quintana A, Hidalgo J, Palacín M, Aparicio P, et al (2023) Splice variants of mitofusin 2 shape the endoplasmic reticulum and tether it to mitochondria. Science (80-). doi: 10.1126/science.adh9351

Nicolas W, Grison M, Trépout S, Gaston A, Fouché M, Cordelières F, Oparka K, Tilsner J, Brocard L, Bayer E (2017a) Architecture and permeability of post-cytokinesis plasmodesmata lacking cytoplasmic sleeve. Nat Plants 3: 17082

Nicolas W, Grison MS, Bayer EMF (2017b) Shaping intercellular channels of plasmodesmata: the structure-to-function missing link. J Exp Bot 69: 91–103

Ostermeyer GP, Jensen KH, Franzen AR, Peters WS, Knoblauch M (2022) Diversity of funnel plasmodesmata in angiosperms: the impact of geometry on plasmodesmal resistance. Plant J 110: 707–719

Otero S, Helariutta Y, Benitez-Alfonso Y (2016) Symplastic communication in organ formation and tissue patterning. Curr Opin Plant Biol 29: 21–28

Pendle A, Benitez-Alfonso Y (2015) Immunofluorescence detection of callose deposition around plasmodesmata sites. Methods Mol Biol 1217: 95–104

Pérez-sancho J, Schapire AL, Botella MA, Rosado A (2016) Analysis of protein-Lipid interactions using purified C2 domains. Methods Mol Biol 1363: 175–187

Pérez-Sancho J, Vanneste S, Lee E, McFarlane H, Esteban del Valle A, Valpuesta V, Friml J, Botella MA, Rosado A (2015) The Arabidopsis SYT1 is enriched in ER-PM contact sites and confers cellular resistance to mechanical stresses. Plant Physiol 168: 132–143

Petit JD, Glavier M, Brocard L, Bayer EM Plasmodesmata ultrastructure determination using electron tomography. Method Mol. Biol.

Platre MP, Mehta P, Halvorson Z, Zhang L, Brent L, Gleason F. M, Faizi K, Goulding C, Busch W (2023) Root Walker: an automated pipeline for large scale quantification of early root growth responses at high spatial and temporal resolution. Plant J. doi: 10.1111/tpj.16493

Platre MP, Satbhai SB, Brent L, Gleason MF, Cao M, Grison M, Glavier M, Zhang L, Gaillochet C, Goeschl C, et al (2021) The receptor kinase SRF3 coordinates iron-level and flagellin dependent defense and growth responses in plants. Nat Com 13: 4445

Prinz WA, Toulmay A, Balla T (2020) The functional universe of membrane contact sites. Nat Rev Mol Cell Biol 21: 7–24

Qian T, Li C, Liu F, Xu K, Wan C, Liu Y, Yu H (2022) Arabidopsis synaptotagmin 1 mediates lipid transport in a lipid composition-dependent manner. Traffic 23: 346–356

Radulovic M, Wenzel EM, Gilani S, Holland LK, Lystad AH, Phuyal S, Olkkonen VM, Brech A, Jäättelä M, Maeda K, et al (2022) Cholesterol transfer via endoplasmic reticulum contacts mediates lysosome damage repair. EMBO J. doi: 10.15252/embj.2022112677

Rowland AA, Chitwood PJ, Phillips MJ, Voeltz GK (2014) ER contact sites define the position and timing of endosome fission. Cell 159: 1027–1041

Ruiz-Lopez N, Pérez-Sancho J, del Valle AE, Haslam RP, Vanneste S, Catalá R, Perea-Resa C, van Damme D, García-Hernández S, Albert A, et al (2021) Synaptotagmins at the endoplasmic reticulum–plasma membrane contact sites maintain diacylglycerol homeostasis during abiotic stress. Plant Cell 33: 2431–2453

Sager R, Wang X, Hill K, Yoo BC, Caplan J, Nedo A, Tran T, Bennett MJ, Lee JY (2020) Auxin-dependent control of a plasmodesmal regulator creates a negative feedback loop modulating lateral root emergence. Nat Commun 11: 1–10

Saheki Y, Bian X, Schauder CM, Sawaki Y, Surma MA, Klose C, Pincet F, Reinisch KM, De Camilli P (2016) Control of plasma membrane lipid homeostasis by the extended synaptotagmins. Nat Cell Biol 18: 504–15

Salvador-Gallego R, Hoyer MJ, Voeltz GK (2017) SnapShot: Functions of endoplasmic reticulum membrane contact sites. Cell 171: 1224.e1-1224.e1

Schauder CM, Wu X, Saheki Y, Narayanaswamy P, Torta F, Wenk MR, De Camilli P, Reinisch KM (2014) Structure of a lipid-bound extended synaptotagmin indicates a role in lipid transfer. Nature 510: 552–555

Schindelin J, Arganda-Carreras I, Frise E, Kaynig V, Longair M, Pietzsch T, Preibisch S, Rueden C, Saalfeld S, Schmid B, et al (2012) Fiji: An open-source platform for biological-image analysis. Nat Methods 9: 676–682

Scorrano L, De Matteis MA, Emr S, Giordano F, Hajnóczky G, Kornmann B, Lackner LL, Levine TP, Pellegrini L, Reinisch K, et al (2019) Coming together to define membrane contact sites. Nat Commun 10: 1287

Simon MLA, Platre MP, Marquès-bueno, Maria M, Armengot L, Stanislas T, Bayle V, Caillaud M, Jaillais Y (2016a) APtdIns(4)P-driven electrostatic field controls cell membrane identity and signalling in plants. Nat Plants 20;2: 16089

Simon MLA, Platre MP, Marquès-Bueno MM, Armengot L, Stanislas T, Bayle V, Caillaud MC, Jaillais Y (2016b) A PtdIns(4)P-driven electrostatic field controls cell membrane identity and signalling in plants. Nat Plants 2: 1–10

Slovak R, Göschl C, Su X, Shimotani K, Shiina T, Busch W (2014) A scalable open-source pipeline for large-scale root phenotyping of Arabidopsis. Plant Cell 26: 2390–2403

Soboloff J, Spassova M a., Dziadek M a., Gill DL (2006) Calcium signals mediated by STIM and Orai proteins-A new paradigm in inter-organelle communication. Biochim Biophys Acta - Mol Cell Res 1763: 1161–1168

Song JH, Kwak S, Nam KH, Schiefelbein J, Lee MM (2019) QUIRKY regukates root epidermal cell patterning through stabilizing SCRAMBLED to control CAPRICE movement in Arabidopsis. Nat Commun 10: 1–12

Song L, Wang Y, Guo Z, Lam SM, Shui G, Cheng Y (2021) NCP2/RHD4/SAC7, SAC6 and SAC8 phosphoinositide phosphatases are required for PtdIns4P and PtdIns(4,5)P2 homeostasis and Arabidopsis development. New Phytol 231: 713–725

Souza PCT, Alessandri R, Barnoud J, Thallmair S, Faustino I, Grünewald F, Patmanidis I, Abdizadeh H, Bruininks BMH, Wassenaar TA, et al (2021) Martini 3: a general purpose force field for coarse-grained molecular dynamics. Nat Methods 2021 184 18: 382–388

Sritharan S, Versini R, Petit J, Bayer E, Taly A (2023) Deep Learning-Based Prediction of A. thaliana's MCTP4 Structure and Exploration of Transmembrane Dynamics using Coarse-Grained Molecular Dynamics Simulations. bioRxiv 2023.08.04.552001

Stahl Y, Faulkner C (2016) Receptor complex mediated regulation of symplastic traffic. Trends Plant Sci 21: 450–459

Stahl Y, Grabowski S, Bleckmann A, Kühnemuth R, Weidtkamp-Peters S, Pinto KG, Kirschner GK, Schmid JB, Wink RH, Hülsewede A, et al (2013) Moderation of arabidopsis root stemness by CLAVATA1 and ARABIDOPSIS CRINKLY4 receptor kinase complexes. Curr Biol 23: 362–371

Tee EE, Johnston MG, Papp D, Faulkner C (2022) A PDLP-NHL3 complex integrates plasmodesmal immune signaling cascades. PNAS 120: e2216397120

Tilsner J, Nicolas W, Rosado A, Bayer EM (2016) Staying Tight: Plasmodesmal Membrane Contact Sites and the Control of Cell-to-Cell Connectivity in Plants. Annu Rev Plant Biol 67: 1–28

Tran TM, McCubbin TJ, Bihmidine S, Julius BT, Baker RF, Schauflinger M, Weil C, Springer N, Chomet P, Wagner R, et al (2019) Maize Carbohydrate Partitioning Defective33 Encodes an MCTP Protein and Functions in Sucrose Export from Leaves. Mol Plant 12: 1278–1293

Tylewicz S, Bhalerao RP, Petterle A, Marttila S, Miskolczi P, Azeez A, Singh RK, Immanen J, Mähler N, Hvidsten TR, et al (2018) Photoperiodic control of seasonal growth is mediated by ABA acting on cell-cell communication. Science 360: 212–215

Vaddepalli P, Herrmann A, Fulton L, Oelschner M, Hillmer S, Stratil TF, Fastner A, Hammes UZ, Ott T, Robinson DG, et al (2014) The C2-domain protein QUIRKY and the receptor-like kinase STRUBBELIG localize to plasmodesmata and mediate tissue morphogenesis in Arabidopsis thaliana. Development 141: 4139–4148

Wang P, Pleskot R, Zang J, Winkler J, Wang J, Yperman K, Zhang T, Wang K, Gong J, Guan Y, et al (2019) Plant AtEH/Pan1 proteins drive autophagosome formation at ER-PM contact sites with actin and endocytic machinery. Nat Commun. doi: 10.1038/s41467-019-12782-6

Wang X, Sager R, Cui W, Zhang C, Lu H, Lee J-Y (2013) Salicylic acid regulates Plasmodesmata closure during innate immune responses in Arabidopsis. Plant Cell 25: 2315–29

Wang Y, Perez-Sancho J, Platre MP, Callebaut B, Smokvarska M, Ferrer K, Luo Y, Nolan TM, Sato T, Busch W, et al (2023) Plasmodesmata mediate cell-to-cell transport of brassinosteroid hormones. Nat Chem Biol June: 1–11

Wilhelm LP, Wendling C, Védie B, Kobayashi T, Chenard M, Tomasetto C, Drin G, Alpy F (2017) STARD 3 mediates endoplasmic reticulum-to-endosome cholesterol transport at membrane contact sites . EMBO J 36: 1412–1433

Wong LH, Levine TP, Wirtz KW, Zilversmit DB, Pagano RE, Vance JE, Bernhard W, Rouiller C, Prinz WA, Vihtelic TS, et al (2016) Lipid transfer proteins do their thing anchored at membrane contact sites… but what is their thing? Biochem Soc Trans 44: 517–27

Wozny MR, Di Luca A, Morado DR, Picco A, Khaddaj R, Campomanes P, Ivanović L, Hoffmann PC, Miller EA, Vanni S, et al (2023) In situ architecture of the ER–mitochondria encounter structure. Nature 618: 188–192

Wu H, Carvalho P, Voeltz GK (2018a) Here, there and everywhere: The importance of ER membrane contact sites. Science 361: 466

Wu S-W, Kumar R, Bagus A, Iswanto B, Kim J-Y (2018b) Callose balancing at plasmodesmata. J Exp Bot

69: 5325–5339

Yan D, Yadav SR, Paterlini A, Nicolas WJ, Petit JD, Brocard L, Belevich I, Grison MS, Vaten A, Karami L, et al (2019) Sphingolipid biosynthesis modulates plasmodesmal ultrastructure and phloem unloading. Nat Plants 5: 604–615

Zavaliev R, Ueki S, Epel BL, Citovsky V (2011) Biology of callose (β-1,3-glucan) turnover at plasmodesmata. Protoplasma 248: 117–130